Preprints (www.preprints.org) | NOT PEER-REVIEWED | Posted: 30 December 2020 doi:10.20944/preprints202012.0750.v1

Research article

A Thermal-Hydraulic Model for the Stagnation of Solar Thermal Systems with Flat-Plate Collector Arrays

Ralph Eismann [1,] *, Sebastian Hummel [2] and Federico Giovannetti [3]

[1] University of Applied Sciences Northwestern Switzerland FHNW; ralph.eismann@fhnw.ch
[2] Technische Hochschule Nürnberg Georg Simon Ohm; sebastian.hummel@th-nuernberg.de
[3] Institut für Solarenergieforschung Hameln (ISFH); giovannetti@isfh.de
* Correspondence: ralph.eismann@fhnw.ch; Tel.: +41-61 228 53 61 (CH)

Abstract: Stagnation is the transient state of a solar thermal system under high solar irradiation where the useful solar gain is zero. Both flat-plate collectors with selective absorber coatings and vacuum-tube collectors exhibit stagnation temperatures far above the saturation temperature of the glycol-based heat carriers within the range of typical system pressures. Therefore, stagnation is always associated with vaporization and propagation of vapor into the pipes of the solar circuit. It is therefore essential to design the system in such a way that vapor never reaches components that cannot withstand high temperatures. In this article, a thermal-hydraulic model based on the integral form of a two-phase mixture model and a drift-flux correlation is presented. The model is applicable to solar thermal flat-plate collectors with meander-shaped absorber tubes and selective absorber coatings. Experimental data from stagnation experiments on two systems, which are identical except for the optical properties of the absorber coating, allowed comparison with simulations carried out under the same boundary conditions. The absorber of one system features a conventional highly selective coating, while the absorber of the other system features a thermochromic coating, which exhibits a significantly lower stagnation temperature. Comparison of simulation results and experimental data show good conformity. This model is implemented into an open-source software tool called "THD" for the thermal-hydraulic dimensioning of solar systems. The latest version of THD, updated by the results of this article, enables planners to achieve cost-optimal design of solar thermal systems and to ensure failsafe operation by predicting the steam range under the initial and boundary conditions of worst-case scenarios.

Keywords: Solar thermal; flat-plate collector; stagnation; steam range; two-phase mixture model; thermal-hydraulic model.

1 Introduction

Solar thermal systems with pressurized circuits for heating, domestic hot water preparation and process heat applications generally use water-glycol mixtures as a frost-resistant heat carrier. In order to prevent the storage tank from overheating, the circulation pump is switched off as soon as the temperature reaches a pre-defined maximum value. Hence, the collector array is no longer actively cooled, and the process of stagnation begins.

Solar thermal systems for the above-mentioned applications are usually operated at a system overpressure below 3 bar which corresponds to saturation temperatures below 140 °C. The maximum stagnation temperature of flat-plate collectors with single glazing and selective absorber coatings can reach above 200 °C. Therefore, stagnation is always associated with the vaporization of the heat carrier. Stagnation is a transient process during which several phenomena occur. After pump shutdown, solar irradiation heats the absorber, thus increasing its temperature and heat losses. The saturation temperature normally is reached near the top of the absorber. In this state, the absorbed solar irradiation is still higher than the heat losses. As a result, the collector turns the excess absorbed

© 2020 by the author(s). Distributed under a Creative Commons CC BY license.

Preprints (www.preprints.org) | NOT PEER-REVIEWED | Posted: 30 December 2020 doi:10.20944/preprints202012.0750.v1

energy with a certain efficiency into vaporization and displacement of the liquid. The rate of these processes depends on the optical and thermal properties of the collector, the boundary conditions and the size of the absorber region at saturation. The major part of the liquid content is displaced into the pipes of the circuit, mostly by volumetric displacement but also by interfacial friction between the increasing steam flow and the liquid. The growing vapor volume displaces an equivalent liquid volume from the circuit into the expansion vessel. The residual liquid within the absorber steadily vaporizes and propagates into the pipes of the circuit. Condensing vapor heats the exposed pipe walls from their initial temperature up to saturation temperature. The vapor propagation into the circuit increases until the enthalpy flow rate of vapor from the collector field drops below the heat losses of the pipes.

The following historical overview shows why stagnation became a research topic relatively late, when solar thermal technology was already well established. Three qualitative ranges of the stagnation phenomenon can be associated with the corresponding collector technologies.

Up to the middle of the 1970s, the vast majority of flat-plate collectors were equipped with non-selective absorbers. The maximum stagnation temperature was about 140 °C, which is below the permissible operation temperature of water-glycol mixtures. This allowed suppression of vaporization by setting the system pressure above saturation pressure.

With the introduction of selective coatings like black-chrome and black-nickel, the efficiency at elevated temperatures was significantly increased. As a result, flat-plate collectors reached a maximum stagnation temperature of up to 180 °C. In most cases, the system pressure was set to values in such a way that the saturation temperature was significantly below the actual temperature during dry stagnation. Vaporization of the liquid and compensation of the vapor volume by a sufficiently large expansion vessel was an accepted strategy to limit the pressure rise during stagnation. Due to the low efficiency in saturation conditions, the steam range was correspondingly small. For this reason and because the market volume was small at the time, the number of failures due to the excessive steam range was too low to merit scientific interest. Pioneering companies solved stagnation problems based on their own expertise and subsequently devised measures, like rules for the arrangement of check valves and the sizing of membrane expansion vessels. Some suppliers proposed suppression of vaporization by a high concentration of glycol and a sufficiently high system pressure.

The adoption of cost-effective, highly selective thin-film absorber coatings in the 1990s and the ensuing market growth led to a dramatic increase in failures caused by the excessive steam range. Typical cases of damage are the loss of liquid caused by the opening of the safety valve, pumps destroyed by the passage of vapor, deformed and thus leaking membranes of expansion vessels due to excessive temperatures and water hammer induced by rapid condensation within the heat exchangers. These phenomena initiated a considerable amount of research dedicated to understanding the stagnation process, to develop measures to limit the steam range and derive theoretical models capable of predicting maximum pressure and steam range.

Terschueren [1] firstly described the stagnation phenomenon qualitatively and recommended useful practical conclusions from observations. In the subsequent years, a series of experimental research projects[2-5] were conducted. Streicher [6] addressed the danger of water hammer induced by rapid condensation. The main objective was to understand and characterize the stagnation process qualitatively and to derive practical rules for the design of collectors and solar thermal systems. Good emptying behavior, characterized by a small quantity of residual liquid within the absorbers, was identified as a decisive prerequisite for a small steam range. Hausner, *et al.* [7] had carried out a comprehensive experimental study on the effect of hydraulic collector design and collector arrangement on the steam range. They introduced the experimental quantity of steam production power, defined as the product of vapor mass flow and the enthalpy of vaporization at the moment of maximum steam range. Their results provided a valuable insight into the influence of hydraulic design and pipe routing on the steam range. They also derived an empirical correlation for the maximum steam range. Its application is limited to the design and operational conditions of the arrangements investigated. In subsequent research projects the influence of collector efficiency and

Preprints (www.preprints.org) | NOT PEER-REVIEWED | Posted: 30 December 2020 doi:10.20944/preprints202012.0750.v1

hydraulic design on maximum steam range was further investigated by Rommel, *et al.* [8],[9] and Scheuren et al.[10], who designed and built an experimental facility with collector fields of different hydraulic design with up to 25.2 m^2 aperture area. Their experiments showed the strong influence of the emptying behavior on the steam range. Based on these experiments Scheuren [11] derived a more general empirical correlation for the steam range. He distinguished three classes of collector fields characterized by good, average and poor emptying behavior and provided a corresponding set of two parameters for the correlation. However, the class needs to be determined initially, based on qualitative considerations and practical experience.

Harrison and Cruickshank [12] and Frank, *et al.* [13] provided a literature review on measures to prevent excessive steam range, covering control strategies, condensers as well as other devices capable of reducing stagnation temperature. They also provided practical examples such as cooling devices, sunshades and collectors with automatic devices such as thermochromic absorber coatings. So far, research has considered stagnation as a succession of five distinguishable processes: heating-up, liquid displacement, vaporization of residual liquid, overheating of the dried-out absorber regions and the re-filling of the collectors.

Eismann [14] used the thermal hydraulic system code TRACE, specifically developed for the safety analysis of nuclear systems [15], to model a solar system consisting of eight flat-plate collectors with meander-type absorbers. The representation of the two-phase states is essentially based on the material data of water and steam. The two-fluid model of TRACE [16] describes both the gas and liquid phases by three one-dimensional conservation equations for mass, momentum and energy. This enables the simulation of two-phase flows in thermodynamic imbalance, for example sub-cooled boiling and condensation.

Simulation results showed that the processes of liquid displacement, vaporization and overheating of dried-out parts of the absorber are, in fact, overlapping. The simulation showed that the phases of displacement and evaporation occur at the same time and that the maximum steam range is reached in an early phase when far less than half of the liquid has evaporated. It was concluded that the maximum steam range can be approximately calculated based on the properties of water and steam, neglecting the effect of fractioned distillation of the water propylene glycol mixture used in the real system. Based on the insight gained, a simplified model was derived. Contrary to the findings of the TRACE simulations, displacement and evaporation were considered as separate processes. These simplifications made it possible to solve the differential equation describing the propagation of steam into the pipes analytically. For the generation of the vapor, only the residual amount of liquid that remained in the absorbers after displacement was considered. This residual quantity was calculated beforehand by a drift-flux model. This model was incorporated in the first version of the open source tool THD [17]. However, experimental validation of the model was not possible at the time. Furthermore, the two-phase model of TRACE is based on the properties of water and steam while the real heat carrier is a mixture of water and propylene glycol. This leads to a considerable uncertainty in the determination of the steam range which motivated further research resulting in the present article. The aim of this article is to derive a model that foregoes the simplifications undertaken earlier.

The new model accounts for the different heat capacities of the steam- and liquid-filled parts of the absorbers and the rise of the saturation temperature as the water content of the water-glycol mixture decreases during evaporation. The new model allows for the fact that displacement and evaporation occur at the same time. The model was calibrated on the basis of stagnation experiments on two real-size solar systems. Section 2 describes the experimental facility and the models to calculate heat losses and state variables not covered by measurements. In section 3, the thermal-hydraulic model for the displacement of liquid from the collector array and the propagation of vapor into the circuit is described. Care has been taken to ensure that the derivations are fully comprehensible, without the need to consult the literature cited.

Preprints (www.preprints.org) | NOT PEER-REVIEWED | Posted: 30 December 2020 doi:10.20944/preprints202012.0750.v1

2 Basic Models and Methods

2.1 *Experimental facility*

At the Institute for Solar Energy Research in Hamelin (ISFH), two identically designed solar thermal systems have been designed and built, dedicated to the experimental analysis of stagnation [18]. The collectors are installed on the roof of an outdoor testing facility, as shown in Figure 1. Both systems have an array of four identically constructed flat-plate collectors, with different absorber coatings. The collectors of one system are equipped with conventional highly selective absorbers, whose optical properties are, in practical consideration, not temperature dependent. The absorber coatings of the other array feature thermochromic behavior.

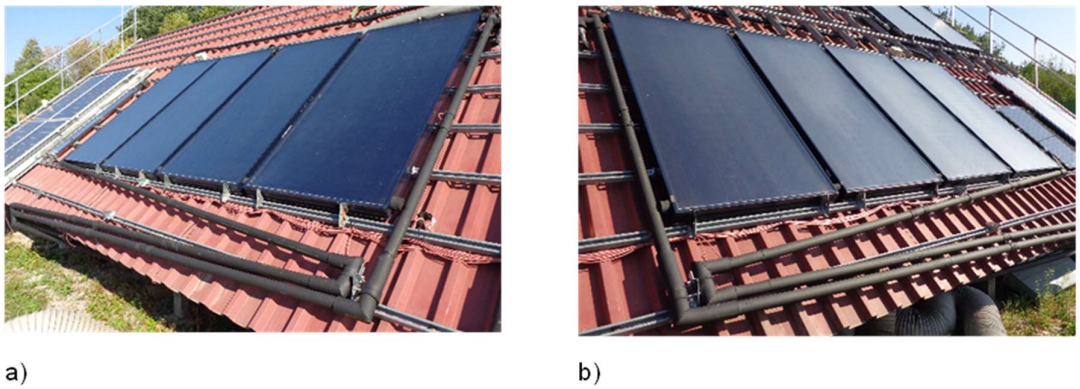

Figure 1 Array of four flat-plate collectors with a) thermochromic absorbers and b) standard selective absorbers.

Below a critical temperature of 68 °C, the emittance of the thermochromic coating is as low as that of a conventional selective absorber. Above the critical temperature, the emittance increases significantly to a much higher value, while the absorptance remains practically constant. This feature considerably lowers the stagnation temperature compared to a conventional selective absorber coating.

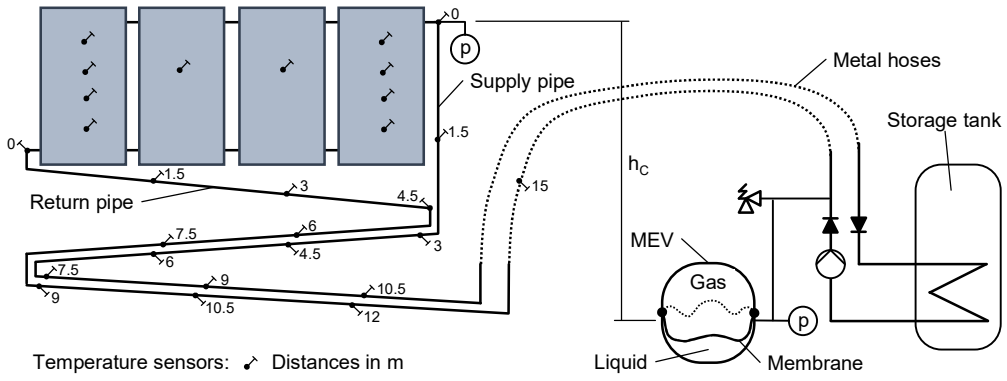

Figure 2 Hydraulic diagram of the circuit, components and temperature sensor positions, valid for both systems.

Figure 2 shows a diagram of the solar circuit and its components. The feed- and return line of the circuit outside the lab building consist of solid copper tubes connected by ferrule fittings made of brass. The pipes are routed in a monotonously downwardly inclined way. Inside the lab-building corrugated metal hoses are used instead of the copper pipes. The height difference between the upper header and the connection to the MEV, which defines the origin of pressure for the circuit, is $h_C = 2.39$

Preprints (www.preprints.org) | NOT PEER-REVIEWED | Posted: 30 December 2020 doi:10.20944/preprints202012.0750.v1

m. The location of the vapor front is detected by measuring the temperature of the pipe wall and the pressure at the collector outlet and at the connection of the membrane expansion vessel. Temperature sensors are attached to the outside of the pipe walls in regular intervals of 1.5 m. The temperature measured is compared to saturation temperature, which indicates the arrival of the vapor front.

Well-defined stagnation experiments were performed in parallel, i.e. under the same boundary conditions, to quantify the effect of different absorber coatings on the steam range and to provide a data set for validation. Ambient air temperature as well as wind speed and the solar irradiation in the collector plane were measured at a location between and immediately above the two collector fields. The properties of the collectors and the material properties of the pipes and insulation layers are listed in Appendix A. A complete set of system data and material properties is given in spreadsheets of the simulation tool. Appendix B offers a list of physical and mathematical quantities and their symbols.

2.2 *Collector design*

The model is derived for flat-plate collectors with meander-shaped absorbers tubes and integrated header tubes as shown in Figure 3. The absorber consists of a copper sheet and meander- and header-tubes made of copper attached to its rear side by laser welding. The total aperture area, A_C, of one collector is composed of the meander tube area, A_M, and the top and bottom header areas, $A_{H,t} = A_{H,b} = A_H$. The top and bottom header regions are identical. V_M and V_H are the volumes of these regions. Four collectors are arranged in a horizontal array and connected in parallel.

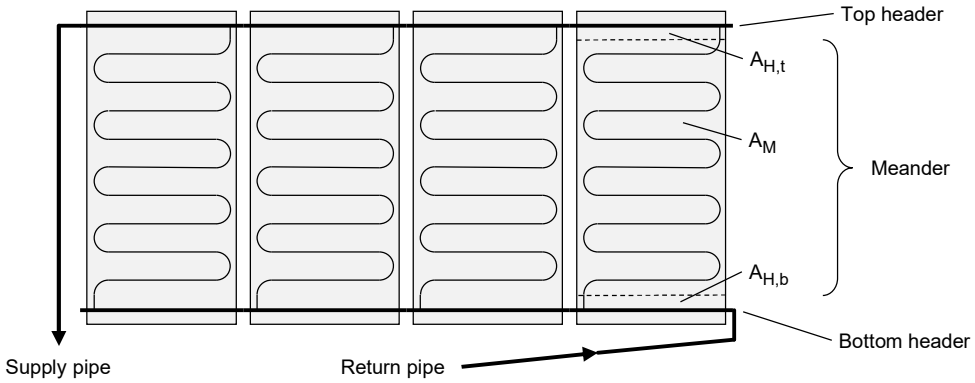

Figure 3 Solar collector array with meander-shaped absorber tubes and integrated header tubes connected in parallel.

2.3 *Collector models*

The stationary useful solar gain of a flat-plate collector with an aperture area, A_C, under constant solar irradiation, G, and ambient temperature, T_a, is calculated by the empirical collector model, Equation (1). Its parameters, the zero-loss efficiency factor, η_0, and the linear and quadratic heat loss coefficients, a_1 and a_2, were determined by a standardized test procedure [19] prior to the stagnation experiments. The expression in brackets represents the efficiency.

$$\dot{Q} = GA_C\left[\eta_0 - \frac{a_1}{G}\left(T_m - T_a\right) - \frac{a_2}{G}\left(T_m - T_a\right)^2\right] \quad (1)$$

Equation (1) is a single node model with the average liquid temperature, T_m, as the only variable of state. The initial temperatures of the circuit components during normal operation prior to stagnation are calculated using this model. The optical properties of a conventional selective absorber are practically constant within the operational range and up to stagnation temperature. Therefore, one set of parameters is sufficient to characterize its efficiency. The characterization of collectors with thermochromic absorbers, however, requires a second set of parameters, $\eta_{0,TC}$, $a_{1,TC}$, and, $a_{2,TC}$.

Preprints (www.preprints.org) | NOT PEER-REVIEWED | Posted: 30 December 2020 doi:10.20944/preprints202012.0750.v1

One set corresponds to the optical properties of a selective absorber whose emittance is very low, e.g. 5%. Above a transition temperature, T_C, the emittance is much higher, e.g. 35%, resulting in much higher thermal losses. The efficiency curves defined by the empirical model and the two sets of parameters intersect approximately at the transition temperature (red dashed lines in Figure 4).

In normal operation, the heat flow within the absorber plate towards the absorber tubes causes a corresponding non-uniform temperature distribution, which results in a higher average absorber temperature and a higher convective heat loss compared to the isothermal case [20]. Consequently, the average fluid temperature at zero solar gain, $T_{\dot{Q}=0}$, is considerably lower than the stagnation temperature of a dry absorber, $T_{S,dry}$, which can be considered locally isothermal. For the same reason, the heat capacity determined experimentally from the transient response is higher than the heat capacity determined from the masses and the corresponding specific heat capacities. On the other hand, vaporization of the liquid also causes a corresponding heat flow within the absorber plate and thus, a temperature distribution different to the locally isothermal case. Therefore, the equilibrium temperature of an absorber section containing evaporating liquid lies between the extremal values for zero solar gain during normal operation and dry stagnation. This temperature is defined by a linear relationship, Equation (2), of the average absorber temperature at zero gain, the stagnation temperature from the test report, and a parameter, K_S. Based on the procedure outlined in section 3.6, a parameter value of $K_S = 0.65$ was determined.

$$T_S = T_{\dot{Q}=0} + K_S \left(T_{S,test} - T_{\dot{Q}=0} \right) \tag{2}$$

In contrast to Equation (1) the efficiency by which a stagnating collector converts the irradiance into the evaporation of the liquid is expressed by a linear function, Equation (3), of the difference between saturation and ambient temperature.

$$\eta = \eta_0 - \frac{U_L}{G}\left(T_s - T_a\right) \tag{3}$$

It is based on the zero-loss efficiency factor, η_0, valid for $T < T_C$ and a heat loss coefficient, U_L, determined by evaluating Equation (3) for $\eta = 0$,

$$U_L = \frac{\eta_0 G_{S,test}}{T_{S,test} - T_{a,test}} \tag{4}$$

Figure 4 shows the efficiency curves for the collector with standard selective and thermochromic absorbers characterized by model parameters listed in **Table 5**, Appendix A.

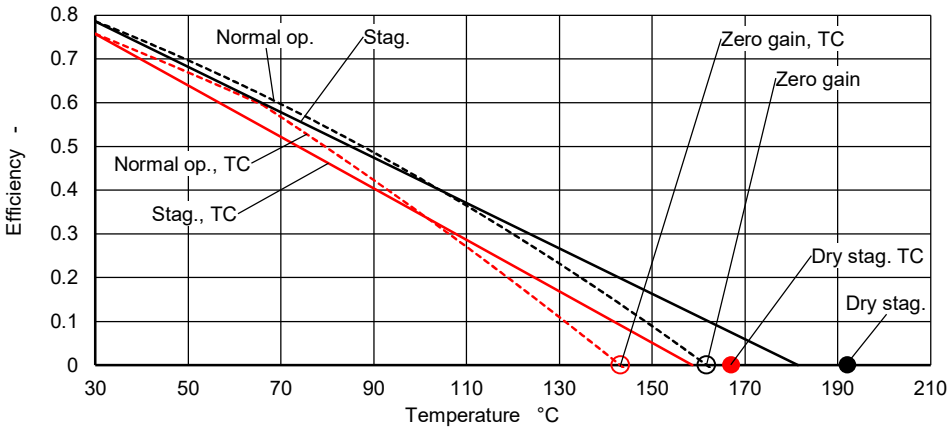

Figure 4 Collector efficiency curves for conventional selective coating (black lines) and thermochromic coating (red lines), valid for G = 1000 W/m² and T_a = 30 °C

Preprints (www.preprints.org) | NOT PEER-REVIEWED | Posted: 30 December 2020 doi:10.20944/preprints202012.0750.v1

2.4 *Heat capacity of different absorber regions*

After the pump is shut down, the circulating liquid no longer cools the collector. The useful solar gain is zero and the temperature of the absorber rises. Heat flow within the absorber during heating-up is caused solely by the inhomogeneity of the heat capacity. Therefore, the local variation of the absorber temperature is negligibly small. In consequence, the heat capacity governing the temperature rise of an absorber after pump shutdown should be calculated solely from the material properties. The contribution of insulation material and the collector casing to the heat capacity is negligible.

The heat capacity of the dry meander region, $C_{M,0}$, and the dry top and bottom header regions, $C_{H,0} \coloneqq C_{H,t,0} = C_{H,b,0}$ are calculated on the basis of the corresponding masses and specific heat capacities. The heat capacity of the liquid-filled absorber is,

$$C_C = C_{M,0} + 2C_{H,0} + \rho_l c_l \left(V_M + 2V_H \right). \tag{5}$$

During liquid displacement and vapor generation, the absorber regions contain residual liquid and saturated vapor. The reduction of steam volume by the very small volume fraction of residual liquid is neglected. With this simplification, the heat capacities of the three absorber regions can be defined as

$$C_X \doteq \left(C_{X,0} + m_{r,X} c_l + \rho_g c_g V_X \right) \tag{6}$$

with index X as H,t, H,b and M, respectively.

2.5 *Heat loss distribution*

Due to convection within the gap between the absorber and the glass cover, the cross-sectional average of the air temperature increases from bottom to top along the slope direction, while the corresponding heat loss coefficient decreases. In addition, the heat losses along the edges are higher than in the center region of the absorber. Both effects are superimposed and result in a temperature distribution in which the maximum is located within the upper third of the absorber. The exact location depends on the width of the air gap, on the heat losses across the edge and on the inclination angle. One collector in each collector array was equipped with four temperature sensors attached to the rear side of the absorber sheet along the middle axis in slope-direction. **Figure 5** shows the normalized temperature distribution during dry stagnation, valid both for both selective and thermochromic coatings. Measured values are indicated by the black markers. Extrapolated values at the positions of the upper and lower header tubes are indicated by transparent markers.

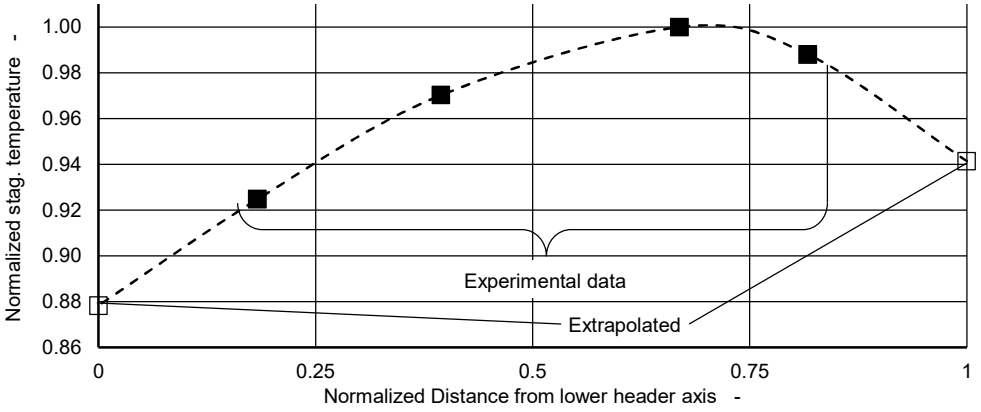

Figure 5 Normalized temperature distribution during dry stagnation, as a function of the distance from the lower header axis. The black markers indicate values measured.

The heat loss at the location with the highest temperature is defined by Equation (3). The average heat loss coefficient for the meander region is calculated using the average of the

Preprints (www.preprints.org) | NOT PEER-REVIEWED | Posted: 30 December 2020 doi:10.20944/preprints202012.0750.v1

experimental values. The heat loss coefficients for the lower and upper header are calculated using the extrapolated values.

$$U_{L,H,b} = U_L \frac{T_S}{T_{H,b}} \quad ; \quad U_{L,M,0} = U_L \frac{T_S}{\langle T_M \rangle} \quad ; \quad U_{L,H,t} = U_L \frac{T_S}{T_{H,t}} \tag{7}$$

2.6 *Supply and return lines*

The supply and return lines are nodalized according to the physical properties, dimensions and orientations of the pipe sections. The dimensions of each pipe section are characterized by their inner diameter, d_t , length, l_t , wall cross-section, A_t , and their orientation, $sin\phi$. Subscripts indicate the section number of the supply line, k, and return line, q , starting with $k = q = 1$ at the collector field. The heat capacities are

$$C_{w,i} = \rho_{t,i} c_{t,i} A_{w,i} l_{t,i} \quad ; \quad C_{l,i} = V_{t,i} \rho_l c_l \quad ; \quad i = k, q \tag{8}$$

The pipes are insulated by rubber foam Armaflex® HT tubes, whose properties are described in the datasheet [21]. Equivalent values are listed in **Table 6**. The inner diameter equals the outer diameter of the pipe, $d_{t,o}$. The outer diameter is denoted by, d_i . The heat capacity of the insulation is ignored.

In order to limit the uncertainties, radiative and convection losses as well as the solar gain of the pipe insulation are modelled in detail. The heat losses of the pipes outside the building are influenced by the solar irradiation absorbed by the surface of the insulation layer and the convective and radiative heat losses to the ambient. The outer surface is assumed to be a Lambertian body. The sky temperature, T_{sky} , is calculated using the model of Swinbank as presented in Adelard, et al. [22]. The environment below the horizon is assumed to be a black body at ambient temperature. The contributions to the infrared radiation heat transfer rate from the insulation surface to the environment are weighted by a viewing-factor, $\gamma = 0.375$, which accounts for shielding of the sky by the contour of the horizon as seen from the position of the pipe.
The Rayleigh, Prandtl and Reynolds numbers are defined for ambient temperature.

$$\mathrm{Ra} = \frac{g L^3 \beta (T_i - T_a) \rho c_p}{\nu \lambda} \quad ; \quad \mathrm{Pr} = \frac{\rho \nu c_p}{\lambda} \quad ; \quad \mathrm{Re} = \frac{wL}{\nu} \tag{9}$$

According to Churchill [23], the Nusselt number for mixed natural and forced convection can be expressed as,

$$\mathrm{Nu} = \left(\mathrm{Nu}_{free}^3 + \mathrm{Nu}_{forced}^3 \right)^{1/3} . \tag{10}$$

The Nusselt number of natural convection from a horizontal cylinder is given by Churchill and Chu [24] , valid for air,

$$\mathrm{Nu}_{hor,free} = \left[0.752 + 0.387 \left(\mathrm{Ra} \cdot 0.401 \right)^{1/6} \right]^2 . \tag{11}$$

According to Gnielinski [25], the Nusselt number for forced convection from a horizontal cylinder can be expressed as a combination of laminar and turbulent contributions,

$$\mathrm{Nu}_{forced} = 0.3 + \sqrt{\mathrm{Nu}_{forced,lam}^2 + \mathrm{Nu}_{forced,turb}^2} , \tag{12}$$

where

$$\mathrm{Nu}_{forced,lam} = 0.664 \sqrt{\mathrm{Re}}\, \mathrm{Pr}^{1/3} \quad ; \quad \mathrm{Nu}_{forced,turb} = \frac{0.037\, \mathrm{Re}^{0.8}\, \mathrm{Pr}}{1 + 2.443\, \mathrm{Re}^{-0.1} \left(\mathrm{Pr}^{2/3} - 1 \right)} \tag{13}$$

Tetsu and Haruo [26] derived a correlation for free convection from a vertical cylinder of the length, l_t ,based on the Nusselt number for free convection from a vertical wall of the same height,

$$\mathrm{Nu}_{vert,free} = \mathrm{Nu}_{plate,free} + 0.435 \frac{l_t}{d} \tag{14}$$

where,

$$\mathrm{Nu}_{plate,free} = \left[0.825 + 0.387 \left(\mathrm{Ra}\, 0.345 \right)^{1/6} \right]^2 , \tag{15}$$

Preprints (www.preprints.org) | NOT PEER-REVIEWED | Posted: 30 December 2020 doi:10.20944/preprints202012.0750.v1

which is also valid for air. The convective heat transfer coefficient is defined as the average of the vertical and horizontal values, weighted by the sine of the inclination angle.

$$\alpha_c = \alpha_{c,vert} \sin\varphi + \alpha_{c,hor}\left(1-\sin\varphi\right) \quad ; \quad \alpha_{c,vert} = \frac{\mathrm{Nu}_{vert}\,\lambda}{l_t} \quad ; \quad \alpha_{c,hor} = \frac{\mathrm{Nu}_{hor}\,\lambda}{d_i} \tag{16}$$

The surface temperature, T_i, of the insulating layer is calculated in a simplified way. The net heat flux is the sum of absorbed solar irradiation, the heat losses through the insulation layer and the heat flux from the surface to the environment by convection and radiation. In a stationary state, the net heat flux at the boundaries to the environment is equal to zero, as expressed by Equation (17).

$$G\alpha_r d_i + \frac{\lambda 2\pi}{\ln\left(d_i/d_{t,o}\right)}\left(T_t - T_i\right) - \alpha_c d_i \pi\left(T_i - T_a\right) - \sigma\varepsilon_s d_i \pi\left[\gamma\left(T_i^4 - T_{sky}^4\right) + \left(1-\gamma\right)\left(T_i^4 - T_a^4\right)\right] = 0 \tag{17}$$

This equation is solved iteratively for the surface temperature. Subsequently, the heat conductivity of the insulation layer, defined as a function of the average temperature, is calculated. Finally, the heat loss coefficient, U_k, for the pipe section, k, related to the temperature difference between the pipe wall and the environment is calculated.

2.7 Pressure maintenance

An expansion vessel with a diaphragm type of membrane and a constant gas content (MEV) serves to maintain pressure. A detailed diagram of the vessel and its location within the circuit is shown in Figure 2. The steel wall of the vessel has a thickness of s = 2.5 mm and a mass of $m_w = 9.5$ kg. The rim of the membrane is attached to the circumference of the inner vessel wall. The diaphragm separates the gas content from the variable liquid content below the membrane.

The pressure jump across the membrane due to its elasticity is considered negligible. In consequence, the pressure of the gas volume and the liquid pressure below the rim are assumed to be identical. The pressure of the water-glycol mixture, indicated in the formulas by WG, at the connection of the MEV is interpreted as the pressure of the gas volume above the membrane.

The nominal gas volume of the empty vessel was determined experimentally as $V_N = 46.6$ liters. The preset pressure, p_0, related to a vessel temperature of $T_0 = 20$ °C was set prior to the filling of the circuit. At the time of pump shutdown, the state of the gas content within the MEV is characterized by a temperature, T, and a pressure, p_{WG}. In this state the vessel contains a liquid volume V_l, which is calculated using the model of the ideal gas.

$$\frac{p_{0,WG} V_N}{T_0} = \frac{p_{WG}\left(V_N - V_l\right)}{T} \quad \Rightarrow \quad V_l = V_N\left(1 - \frac{p_{0,WG} T}{p_{WG} T_0}\right) \tag{18}$$

The pressure within the upper header of the collector is,

$$p_{H,WG} = p_{WG} - \rho g h_H \,. \tag{19}$$

The stagnation model is based on the properties of water and steam. It is therefore necessary to transform the pressure measured at the top of the collector array, $p_{H,WG}$, so that vaporization of water begins at the same temperature as vaporization of the heat transfer liquid TyfocorLS® used in the experiments. For this purpose, numerical routines for the vapor pressure of water, $p_v\left(T\right)$, as a function of temperature and the saturation temperature of TyfocorLS®, $T_{s,WG}\left(p\right)$, as a function of saturation pressure were implemented. The corresponding saturation pressure of steam is,

$$p_H = p_v\left[T_{s,WG}\left(p_{H,WG}\right)\right] \,. \tag{20}$$

The corresponding pressure of the gas volume within the MEV is,

$$p = p_H + \rho g h_H \,. \tag{21}$$

Finally, the corresponding preset pressure for water, p_0, at the reference temperature, T_0, is calculated to be,

$$p_0 = \frac{p T_0\left(V_N - V_l\right)}{V_N T} \,. \tag{22}$$

Preprints (www.preprints.org) | NOT PEER-REVIEWED | Posted: 30 December 2020 doi:10.20944/preprints202012.0750.v1

With increasing vapor volume during stagnation, hot liquid from the circuit is displaced into the MEV. As a result, the gas temperature increases. The gas temperature, T_g, is calculated by a model using the following simplifications. The vessel is represented by a sphere of the same nominal volume, V_N, and a corresponding diameter which represents the characteristic length, L. The liquid content and the associated lower half sphere of the vessel wall are considered isothermal. An emittance of $\varepsilon = 1$ is assumed for both the MEV and the environment. The emittances of the membrane and the inside of the steel wall are defined as $\varepsilon_M = 1$ and $\varepsilon_W = 0.5$. The convective heat transfer between vessel wall and ambient are calculated by Raithby and Hollands [27].

$$\mathrm{Nu} = 0.56\left[\left(\mathrm{Ra}\,\mathrm{Pr}/\left(0.846+\mathrm{Pr}\right)\right)\right]^{1/4} + 2 \tag{23}$$

The convective heat transfer across the gas volume between membrane and the vessel wall is estimated using the correlation of Dropkin and Somerscales [28] for 45° inclined cavities heated from below.

$$\mathrm{Nu} = 0.0059\,\mathrm{Ra}^{0.33}\,\mathrm{Pr}^{0.074} \tag{24}$$

Heat conduction between the two isothermal vessel shells is estimated using d/3 as the equivalent length,

$$\dot{Q} = \frac{\lambda}{d/3} sd\pi\left(T_l - T_W\right) \tag{25}$$

In a first step, the temperature change of the liquid content due to the ingress of hot liquid from the expansion line is calculated. In a second step, the temperature changes due to convective and radiative heat losses during the time interval, τ, are determined. Finally, the average temperature of the gas content is calculated.

2.8 Properties of the liquid and gaseous phase within the circuit

The heat carrier liquid TyfocorLS® used in the experiments is a mixture of water, propylene glycol and anti-corrosion additives with a mass fraction of water, x_m = 0.58. Figure 6 shows the phase diagram of a binary mixture of water and propylene glycol as a function of the molar fraction, x, calculated for a total pressure of 3 bar. Apparently, the vapor phase of the original mixture with a mass fraction of water, x_m = 0.58 consists practically only of the vapor of water. Even at the dry stagnation temperature of the thermochromic collector, 167 °C, and the selective collector, 192 °C, the molar fraction of propylene glycol is quite small. It can be concluded from the diagram that the collector will never dry out entirely because the saturation temperature of pure propylene glycol will never be reached.

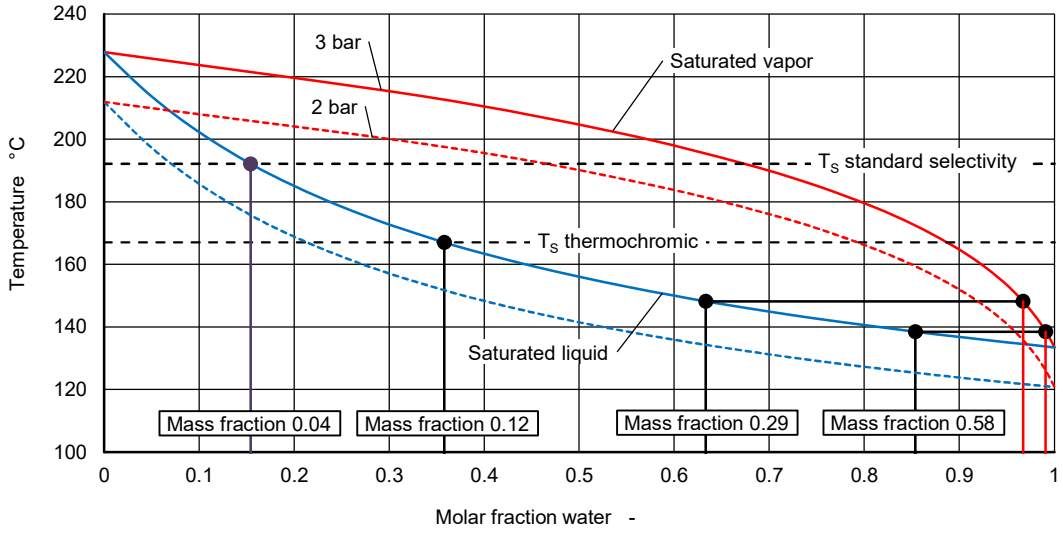

Figure 6 Phase diagram of water propylene glycol at 3 bar absolute pressure.

Preprints (www.preprints.org) | NOT PEER-REVIEWED | Posted: 30 December 2020 doi:10.20944/preprints202012.0750.v1

The features stated above justify the following simplifications:

- The efficiency of the absorber region is defined by the saturation temperature of the residual liquid, $T_{s,r}$, which itself is a function of the water content.
- The glycol content of the vapor is ignored. Henceforth, the gas phase is referred to as steam.
- Contribution of the overheated regions of the absorber to the energy balance is neglected.
- The pressure and the fluid properties of the original mixture define the saturation temperature of steam within the pipes.

The saturation temperature of the liquid increases as the water content vaporizes during stagnation. The current mass fraction of water is calculated from the initial residual mass and the mass fraction of the original mixture, x_{m0},

$$x_m = \frac{m_r}{m_r + m_{r,G}} = \frac{m_r}{m_r + m_{r0}\dfrac{1-x_{m0}}{x_{m0}}} \quad . \tag{26}$$

The molar fraction needed for the calculation of the saturation pressure is,

$$x = \frac{m_r/M_W}{m_r/M_W + m_{G0}/M_G} = \frac{x_m/M_W}{x_m/M_W + (1-x_{m0})/M_G} \tag{27}$$

The saturation temperature of the liquid, $T_{s,r}$, is iteratively calculated by applying Raoult's law,

$$p_s = x\,p_{v,W} + (1-x)\,p_{v,G} \tag{28}$$

2.9 *Time evolution of circuit temperatures*

The time evolution of the temperature in each pipe section is calculated in a three-step procedure within a succession of equidistant time steps. In each time step, the liquid-filled part of a pipe section is considered as isothermal. In a first step, the temperature change due to the displaced liquid is calculated. If the general flow direction in normal operation is from the bottom to the top within each collector of a collector array, then about $R_D = 0.8$ of the fluid content is displaced via the return line during stagnation, regardless of the hydraulic design. This remarkable result was found experimentally by Hausner, Fink, Wagner, Riva and Hillerns [7] and confirmed by Eismann [14] via TRACE simulations. The average temperatures of the liquid filled pipe section, q, of the return line at the time step, j,

$$T_{q,j} = T_{q,j-1} + \frac{\left[C_{w,q} + \left(V_q - R_D\Delta V_j\right)\rho_l c_l\right]T_{q,j-1} + R_D\Delta V_j\,\rho_l c_l T_{q-1,j-1}}{\rho_l c_l V_q + C_{w,q}} \quad , \tag{29}$$

are subsequently calculated, beginning with the pipe section, $q = 1$, connected to the inlet of the collector array. The average temperatures of the supply line sections, k, are calculated in the same way while R_D is replaced by $1 - R_D$. As shown by simulation results, the total volume of liquid displaced into the supply line and the maximum steam volume in the supply line are much less than the volume of the helical coil heat exchanger of about 10 l. It is therefore assumed that the temperature of the liquid leaving the heat exchanger towards the reference point is constant and equal to the initial temperature of the return line. The average temperatures of the expansion line section and of the liquid content of the MEV are calculated analogously. In a second step, new heat loss coefficients are determined. Finally, the temperature change within the same time step due to heat losses into the ambient is calculated.

2.10 *Two-phase mixture model*

In this section a detailed two-phase mixture model is presented. The model is based on the integral form of the energy and mass conservation equations (30) and (31). The following assumptions were taken: The temperature of the gas and liquid phase are the same; phase change is caused only by heat transfer across the pipe wall; Kinetic and potential energy are ignored so that the

Preprints (www.preprints.org) | NOT PEER-REVIEWED | Posted: 30 December 2020 doi:10.20944/preprints202012.0750.v1

mass-specific total energy can be substituted by the mass-specific inner energy, u_l and u_g, of the liquid and gas phase. In the three-dimensional formulation, the state variables and the fluid properties are local quantities. The phase indicator function, ε, indicates the presence of a gas phase, $\varepsilon = 1$, or liquid phase, $\varepsilon = 0$. The energy conservation equation (30),

$$\begin{aligned} \iiint_V \frac{\partial}{\partial t}\left[\varepsilon\rho_g u_g + (1-\varepsilon)\rho_l u_l\right]dV + \iint_{S_C}\left[\varepsilon\rho_g u_g \vec{w}_g + (1-\varepsilon)\rho_l u_l \vec{w}_l\right]\vec{n}dS \\ = \sum \dot{Q} - \iint_S p\left(\varepsilon\vec{w}_g + (1-\varepsilon)\vec{w}_l\right)\vec{n}dS \end{aligned} \quad , \tag{30}$$

consists of four parts. The volume integral accounts for the change of internal energy within the collector volume. The surface integral on the left-hand side describes the flow of inner energy across the boundary, i.e. the cross-section of the inlet and outlet, of the collector field or a pipe section. The first term on the right-hand side represents the energy flux exchanged with the ambient. The second term on the right-hand side is the displacement power exercised at the inlet and outlet ports. The mass conservation equation is defined as,

$$\iiint_V \frac{\partial}{\partial t}\left[\varepsilon\rho_g + (1-\varepsilon)\rho_l\right]dV + \iint_S\left[\varepsilon\rho_g \vec{w}_g + (1-\varepsilon)\rho_l \vec{w}_l\right]\vec{n}dS = 0 \quad . \tag{31}$$

Since the pressure losses are ignored, the momentum conservation equation can be replaced by a static pressure balance. The pressure of the saturated steam is determined by the temperature of the gas content, $T_{g,MEV}$, and the liquid volume, V_l, inside the MEV and the height, h_v, of the liquid column above the MEV.

$$p = \frac{p_0 V_N}{V_N - V_l}\frac{T_{g,MEV}}{T_0} - \rho g h_v \tag{32}$$

Further simplifications introduced in the following sections allow the integration of Equations (30) and (31). Integration transforms the phase indicator function, ε, into the macroscopic void fraction, which is denoted by the same symbol.

$$\varepsilon := \frac{V_g}{V_g + V_l} = \frac{V_g}{V} \quad . \tag{33}$$

2.11 Drift-flux correlation

In a mixture model, the effect of interfacial friction on the void fraction caused by different phasic velocities must be modelled with an additional correlation. One of the most successful approaches is the drift-flux model originally developed by Zuber and Findlay [29], which is presented in a simplified way as follows. The local drift velocity, w_{gj}, is defined as the difference between the local velocity of the gas phase, w_g, and the sum of the superficial velocities of the gas and liquid phases, j_g and j_l.

$$w_{gj} = w_g - \left(j_g + j_l\right) = \frac{j_g}{\varepsilon} - \left(j_g + j_l\right) \tag{34}$$

Multiplying both sides by the local void fraction and averaging over the cross-section of the pipe yields,

$$\left\langle \varepsilon w_{gj} \right\rangle = \left\langle j_g \right\rangle - \left\langle \varepsilon\left(j_g + j_l\right)\right\rangle \quad . \tag{35}$$

On both sides of the equation the average of products is replaced with the product of averages, which requires the introduction of a phase distribution parameter, C_0, and a corrected average drift velocity, U_{gj}.

$$\langle\varepsilon\rangle U_{gj} = \left\langle j_g \right\rangle - C_0 \langle\varepsilon\rangle\left(j_g + j_l\right) \tag{36}$$

Solving Equation (36) for the cross-sectional average of the void fraction yields the cross-sectional average of the void fraction,

Preprints (www.preprints.org) | NOT PEER-REVIEWED | Posted: 30 December 2020 doi:10.20944/preprints202012.0750.v1

$$\langle \varepsilon \rangle = \frac{\langle j_g \rangle}{C_0 \langle j_g + j_l \rangle + U_{gj}} \quad . \tag{37}$$

In the subsequent formulas, the brackets indicating averages are omitted. Many correlations have been developed for various flow geometries and boundary conditions. A comprehensive overview is given by Coddington and Macian [30] . The correlations of Choi, *et al.* [31], applicable to pipe inclinations from upward-vertically to downward-vertically oriented circular pipes, were found to sufficiently suitable for the purpose of this model. The phase distribution parameter is defined as,

$$C_0 = \frac{2}{1+\left(\mathrm{Re}/1000\right)^2} + \frac{1.2 - 0.2\sqrt{\rho_g/\rho_l}\left(1-\exp\left(-18\varepsilon\right)\right)}{1+\left(1000/\mathrm{Re}\right)^2} \quad . \tag{38}$$

The two-phase Reynolds number is,

$$\mathrm{Re} = \frac{\left(j_g + j_l\right) d_t}{\nu_l} \quad . \tag{39}$$

For the average drift velocity, they developed an extended form of the Zuber and Findlay correlation that accounts for the effect of the inclination angle.

$$U_{gj} = 0.0246 \cdot \cos\varphi + 1.606 \cdot \sin\varphi \left[\frac{\left(\rho_l - \rho_g\right)\sigma g}{\rho_l^2} \right]^{1/4} \tag{40}$$

The correlations of the phase distribution parameter and the average drift velocity are calibrated by data from stationary experiments with non-zero superficial velocities. With an appropriate correction presented later in section 3.1.1, the model can be used to estimate the void fraction at the limit of vanishing liquid superficial velocity. The liquid holdup is complementary to the void fraction and a measure for the amount of residual liquid.

$$\varepsilon_l = 1 - \varepsilon \tag{41}$$

The residual liquid mass of the water-glycol mixture is,

$$m_{r0,WG} = \rho_{l,WG} \cdot V \left(1 - \varepsilon\right) \tag{42}$$

The residual mass of water is,

$$m_{r0} = x_{m0} \cdot m_{r0,WG} \tag{43}$$

3 Derivation of the model

3.1 Residual liquid

Calculation of the amount of residual liquid is decoupled from the transient model. It is determined on the basis of state variables and boundary conditions that occur when the saturation temperature is reached, and the following simplifying assumptions:

1. The meander and header tubes are completely wetted. All parts of the absorber contribute to vaporization according to their efficiency.
2. Only steam leaves the wetted and steam-filled parts of the absorber. The residual liquid is considered stationary, which is expressed by a liquid superficial velocity of $j_l = 0$ everywhere in the absorber.
3. The influence of two-phase pressure losses on the saturation temperature is ignored. In consequence, each absorber within the collector array undergoes the same process and the saturation temperature is the same everywhere.
4. The steam flow distributions in the upper and lower parts of the absorber are symmetrical.

Meander and header tubes are treated separately. The length and the volume of the pipe bends in the meander tube are added to the straight parts. A meander with a total length, l_M , is nodalized into $2n$ straight, horizontal pipe sections. The numbering of absorber pipe sections starts at the middle of the meander tube from $k = 1$ to n_M in both upstream and downstream direction. It follows from

Preprints (www.preprints.org) | NOT PEER-REVIEWED | Posted: 30 December 2020 doi:10.20944/preprints202012.0750.v1

assumptions 2, 3 and 4 that the steam flow distributions in the upper and lower parts of the absorber are symmetrical.

The superficial velocity of the steam flow is proportional to the section number, k, as calculated from the mass and energy balance,

$$j_{g,k} = \frac{4\dot{m}_k}{\rho_g d_{t,M} \pi} = \frac{4GA_M \eta_{s,M} k}{d_{t,M} \pi 2 n_M h_v \rho_g} \quad , \tag{44}$$

The efficiency of the meander region is,

$$\eta_{s,M} = \eta_0 - U_{L,M} \left(T_s - T_a \right) = 0 \tag{45}$$

Inserting into Equation (37) and using Equation (41) yields the liquid holdup of the water-glycol mixture,

$$\varepsilon_{l,WG,k} = \left(1 - \varepsilon_{WG,k} \right) \quad . \tag{46}$$

The total amount of residual water in the meander tube is calculated using the initial mass fraction of water, x_{m0}, and totaling over all the meander tube sections,

$$m_{r0,M} = x_{m0} m_{r0,M,WG} = x_{m0} 2 \rho_l V_M \sum_{k=1}^{n_M} \left(1 - \varepsilon_{WG,k} \right) \quad . \tag{47}$$

Since the absorber area associated with a header is small compared to the meander region, their contribution to the vaporization is also small. It is therefore sufficient to describe each header tube by a single node. The superficial velocity in the k^{th} upper header tube results from the total quantity of steam flows in the upper half of 1 to k meanders and the steam flows in 1 to k header tubes,

$$j_{g,k} = \frac{4G\left(A_M / 2 + A_H \right) \eta_{s,H,t} k}{d_{t,H} \pi h_v \rho_g} \quad . \tag{48}$$

Inserting Equation (48) into Equation (37) yields the void fraction. The residual mass is calculated using Equation (47). The residual mass of the water-glycol mixture in the k^{th} bottom header tube is calculated analogously.

3.1.1 Corrections for the residual mass of water

The simplifying assumptions 2 and 4 stated in the section above were a pre-requisite for the calculation of the initial residual mass. However, the liquid content will move during the stagnation process under the influence of gravity and friction between the steam flow and the liquid. A portion of the initial residual quantity will leave the absorber in liquid form and therefore not contribute to the steam flow entering the pipes. The magnitude of this proportion is estimated considering the following effects:

If the collector efficiency is high, the vaporization rate and the steam velocity are also high. Interfacial friction dominates and the effect of gravity on the liquid content within the pipe bends can be ignored. The predominant proportion of the residual liquid evaporates while only a small proportion leaves the collector in liquid form.

At low efficiencies, however, the vaporization rate is small. In consequence, the interfacial friction is weak and phase separation is more pronounced. As a result, nearly all the liquid is displaced via the return line. A larger proportion of the residual liquid entering the pipe bends of the upper regions of the absorber flows downwards against the weak steam flow. The liquid within the meander tube slowly accumulates in lower regions where the heat losses are higher. The smaller proportion of the residual liquid evaporates while the predominant fraction leaves the collector in liquid form, propelled by the weak interfacial friction and gravity. Based on this hypothesis and the procedure outlined in section 3.6, the following distribution function was derived, which describes the ratio of the liquid mass that evaporates during stagnation to the initial residual mass as calculated by the drift-flux correlation.

$$\delta = 0.02 + \left(0.7 - 0.02 \right) \left[1 - \exp\left(-240 \cdot \eta_{M,0}^{\left(2.28 + 4\eta_{M,0} \right)} \right) \right] \tag{49}$$

Preprints (www.preprints.org) | NOT PEER-REVIEWED | Posted: 30 December 2020 doi:10.20944/preprints202012.0750.v1

The same distribution function is used to correlate the probable center of the residual liquid with the corresponding local heat loss coefficient,

$$U_{L,M} = U_{L,H,b} + \delta\left(U_{L,M,0} - U_{L,H,b}\right) \tag{50}$$

The relevant part of the residual water contributing to the steam range is,

$$m_{r0,M} = \delta x_{m,0} \cdot m_{r0,M,WG} \tag{51}$$

3.2 *Temperature rise*

After pump shutdown the absorber is heated up by the solar gain. The temperature rise is not uniform, due to the increased heat losses across the edges of the collector and along the flow path. However, the model for the displacement phase, which is derived in section 3.2, requires the assumption of a linear absorber temperature distribution within the liquid-filled part, which simplifies the modelling tremendously. It follows from this simplification that boiling commences as soon as the outlet reaches saturation temperature, T_s. The temperature rise during the heating-up period is described by Equation (52), where T is the temperature of the absorber at an arbitrary location along the flow path.

When dimensioning solar thermal systems, the maximum steam range should be determined for extremal but constant values of solar irradiation and ambient temperature. The elapsed time between pump shutdown and the onset of boiling is irrelevant. For comparison of simulations and experiments under varying boundary conditions, however, onset of boiling should coincide with experimental data, because the boundary conditions are time-dependent. A correction factor, $K_h = 0.8$, accounts for the fact that the temperature within the meander region rises faster than the average temperature.

$$K_h C_C \dot{T} + U_L A_C \left(T - T_a\right) = G A_C \eta_0 \tag{52}$$

It is sufficient to solve this equation numerically using the Euler method. For $G\eta_0 > U_L\left(T_s - T_a\right)$, the temperature at the absorber outlet, T_ω, reaches saturation temperature, T_s, within a finite time interval.

With the onset of boiling three processes start to run in parallel. The growing steam volume displaces the liquid content from the absorber into the connecting pipes. The regions below saturation temperature are heated up by the solar gain and the displaced liquid from regions with higher temperature. At the same time, steam leaves the absorber and enters the pipes. Describing these combined processes using the two-phase mixture model requires further simplifications. Time evolution of the state variables is assumed as identical in each collector of the collector array. In consequence, the mass flows of displaced liquid and of steam entering the adjoining pipes are proportional to the number, n, of collectors. It is adequate to describe liquid displacement and steam generation independently, based on the following definitions and simplifications illustrated by Figure 7.

Liquid displacement happens simultaneously in the upper header, the lower header and the meander tube. It is therefore not necessary to distinguish between these three regions. This allows the description of the processes of displacement and steam generation in one dimension as a function of the volume, V.

Preprints (www.preprints.org) | NOT PEER-REVIEWED | Posted: 30 December 2020 doi:10.20944/preprints202012.0750.v1

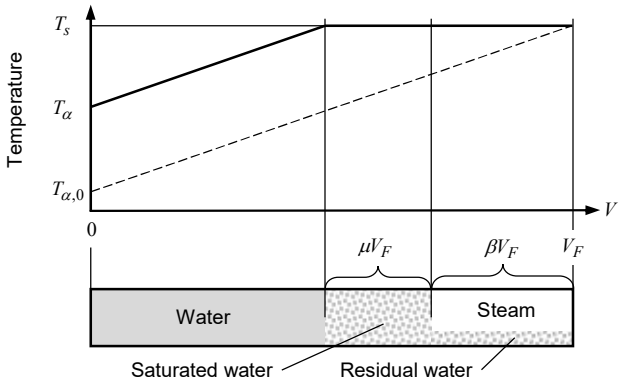

Figure 7 Thermodynamic states within a stagnating collector field during displacement.

The temperature gradient within the region below saturation temperature results from normal operation prior to pump shutdown,

$$\frac{dT}{dV} = \frac{T_\omega - T_\alpha}{V_F} \quad , \tag{53}$$

and is defined as a constant during the whole displacement process. The sizes of three volume fractions and the corresponding absorber areas are defined using parameters, μ and β, between 0 and 1.

The volume part, βV_F, contains steam and residual water. The solar gain of the corresponding absorber area, βA_F, causes vaporization and, if the pressure increases, a corresponding increase in temperature. Only saturated steam generated in this region contributes to the steam flow from the collector into the adjoining pipes.

The volume part, μV_F, contains saturated water. Steam generated in this region of the absorber only contributes to the displacement of liquid. The simplifying assumption of a constant heat loss allows the definition of the parameter, μ, as a function of the time dependent inlet temperature, T_α.

$$\mu := \begin{cases} \dfrac{T_{s,r} - T_\alpha}{T_{s,r} - T_{\alpha,0}} & ; \quad \mu + \beta < 1 \\ 1 - \beta & ; \quad \dfrac{T_{s,r} - T_\alpha}{T_{s,r} - T_{\alpha,0}} + \beta > 1 \end{cases} \tag{54}$$

The temperature rises in a linear fashion along the coordinate, V, from the actual temperature, T_α, at the collector inlet, $V = 0$, to saturation temperature at $V = \lambda V_F$.

$$\lambda = \begin{cases} 1 - \beta - \mu & ; \quad \beta + \mu < 1 \\ 0 & ; \quad \beta + \mu = 1 \end{cases} \tag{55}$$

By using the definitions stated by Equation (54) and Equation (55), Equation (30) can be represented by two coupled equations describing liquid displacement and steam generation as follows.

3.3 *Liquid displacement*

Equation (56) is the one-dimensional representation of Equation (30) describing liquid displacement.

$$\int_0^{\mu V_F} \frac{\partial}{\partial t}\left[\varepsilon_\mu \rho_g u_g + \left(1 - \varepsilon_\mu\right)\rho_l u_l\right] dx + \dot{m}_l u_l = \mu\left(G A_F \eta_s - n_C \frac{\partial}{\partial t}\left(C_C T_s\right)\right) - \dot{m}_l \frac{p}{\rho_l} \quad . \tag{56}$$

The first term on the right-hand side represents the part of the solar gain transferred to the saturated liquid within the region, μV_F, of the absorber content, which causes steam generation. By application of the one-dimensional form of the mass conservation equation,

Preprints (www.preprints.org) | NOT PEER-REVIEWED | Posted: 30 December 2020 doi:10.20944/preprints202012.0750.v1

$$\int_0^{\mu V_F} \frac{\partial}{\partial t}\left[\varepsilon_\mu \rho_g + \left(1-\varepsilon_\mu\right)\rho_l\right] dx + \dot{m}_l = 0 \quad , \tag{57}$$

the derivative of the void fraction can be replaced by the mass flow of displaced liquid.

$$\dot{m}_l = \frac{\mu\left[GA_F\eta_s - n_C\frac{\partial}{\partial t}\left(C_C T_s\right)\right]\left(\rho_l - \rho_g\right)}{\rho_g h_v} \tag{58}$$

In order to integrate this equation analytically over short time periods, the heat capacity of the collector is set as a constant and the derivative of the saturation temperature of steam is replaced by the finite difference ratio of values from the preceding time step.

$$\Delta C_{C,j} := n_C\frac{\partial}{\partial t}\left(C_C T_s\right) \approx n_C C_C \frac{T_{s,j} - T_{s,j-1}}{t_{s,j} - t_{s,j-1}} \tag{59}$$

The growth rate of the overall void fraction r can be obtained from the mass balance applied on the whole absorber.

$$\dot{\varepsilon} = \frac{\dot{m}_l}{V_F\left(\rho_g - \rho_l\right)} \tag{60}$$

Integration over time yields the void fraction and, finally, the actual steam volume, $V_v = \varepsilon V_F$. The parameter, β, describing the steam-filled part of the collector array is defined as a function of the steam volume and the total residual mass of water:

$$\beta := \frac{V_v}{\left(1-\varepsilon_r\right)V_F} = \frac{\varepsilon}{1-\varepsilon_r} \quad ; \quad \varepsilon_r = \frac{m_r}{V_C\rho_l} \tag{61}$$

3.4 Steam generation

The model for steam generation is based on the following considerations. The vaporization rate, $\dot{m}_r$, of residual liquid depends on the solar gain at saturation temperature and the change of enthalpy of the absorber due to change of the saturation temperature of the residual liquid, $T_{s,r}$. The time evolutions of the vaporization rate within the absorber and the header tubes are different because the initial residual masses and the respective absorber areas are not the same. It is therefore necessary to calculate the vaporization rate for the meander and the upper and lower headers separately, while the same parameter, β, is used for all regions. In order to simplify mathematical expressions, the model will be derived for an unspecified region, A_X, of one single absorber.

Displacement of liquid is usually accompanied by an increase in pressure, hence an increase in saturation temperature. Therefore part of the absorbed energy within the region, βV_X, is used for the heating-up of the absorber. The steam generation rate within the absorber region depends on the current mass of residual water within this region, $m_{r,X}$. If $m_{r,X} = m_{r0,X}$, the absorber region is assumed to be fully wetted and the whole steam-filled region contributes to steam generation. Steam generation decreases with a decreasing residual mass of water. It is therefore reasonable to quantify the proportion of the steam-filled region contributing to steam generation as a function of the current mass related to the initial mass of the residual water, $\left(m_{r,X}/m_{r0,X}\right)^\alpha$. The value of the exponent, α, is defined later. Thus, the total power attributed to vaporization is,

$$\dot{Q}_{v,X} = \left(GA_X\eta_{s,r} - \frac{\partial}{\partial t}\left(C_X T_{s,r}\right)\right)\beta\left(\frac{m_{r,X}}{m_{r0,X}}\right)^\alpha \quad . \tag{62}$$

The goal is to find a formula for the steam power, i.e. the enthalpy flow of steam leaving the absorber, as a function of time. By definition, steam generated within the volume fraction of the region, βV_X, contributes only to the outflow of steam from the collector field. Therefore, the surface integral on the left-hand side of Equation (30) reduces to $\dot{m}_g u_g$ and the surface integral on the right-hand side of the same equation to $\dot{m}_g p/\rho_g$. Thus, the one-dimensional form of Equation (30) becomes,

Preprints (www.preprints.org) | NOT PEER-REVIEWED | Posted: 30 December 2020 doi:10.20944/preprints202012.0750.v1

$$\int_0^{\beta V_X} \dot{\varepsilon}_X \left[\rho_g u_g - \rho_l u_l\right] dx + \dot{m}_{g,X} u_g = \left(GA_X \eta_X - \frac{\partial}{\partial t}\left(C_X T_{s,X}\right)\right) \beta \left(\frac{m_{r,X}}{m_{r0,X}}\right)^{\alpha} - \dot{m}_{g,X} \frac{p}{\rho_g} \tag{63}$$

Integration and replacing specific inner energies by specific enthalpies, $u = h - p/\rho$, yields,

$$\beta V_X \dot{\varepsilon}\left(\rho_g h_g - \rho_l h_l\right) + \dot{m}_{g,X} h_g = \left(GA_X \eta_X - \frac{\partial}{\partial t}\left(C_X T_{s,X}\right)\right) \beta \left(\frac{m_{r,X}}{m_{r0},X}\right)^{\alpha} \tag{64}$$

The void fraction and its derivative are defined by the residual mass and the mass fraction of water.

$$\varepsilon_X = 1 - \frac{m_{r,X}}{\rho_l \beta V_X x_{m,X}} \quad \Rightarrow \quad \dot{\varepsilon}_X = -\frac{\dot{m}_{r,X}}{\rho_l \beta V_X x_{m,X}} \tag{65}$$

Since the densities of water and propylene glycol above 100°C differ by less than 2%, it is sufficient to base the void fraction on the density of the saturated water. The mass flow of steam can be expressed by the derivative of the residual liquid by applying the mass balance, Equation (31), to the region, *X*.

$$\dot{m}_{g,X} = -\dot{m}_{r,X} \left(\frac{\rho_l - \rho_g}{\rho_l}\right) \tag{66}$$

Inserting into Eq.(64) yields the differential equation for the residual liquid mass.

$$\dot{m}_{r,X} = -m_{r,X}^{\alpha} \frac{\beta\left(GA_X \eta_X - \frac{\partial}{\partial t}\left(C_X T_{s,X}\right)\right)}{h_v m_{r0,X}^{\alpha}} \tag{67}$$

Since the saturation temperature varies only slowly with pressure, the equation can be integrated over a sufficiently short time interval, $t_j - t_{j-1}$. The derivative of stored heat is replaced by the finite difference with values from the previous interval. The specific enthalpies of steam are evaluated at the saturation temperature of the liquid.

$$\frac{\partial}{\partial t}\left(C_X T_{s,X}\right) \approx \Delta C_{X,j} = \frac{\left(C_{X,0} + m_{r,X,j} c_l\right)\left(T_{X,j} - T_{X,j-1}\right) + V_X\left(\rho_{g,j} h_{g,j} - \rho_{g,j-1} h_{g,j-1}\right)}{t_j - t_{j-1}} \tag{68}$$

It is reasonable to assume that dry out is reached within a finite time interval, which requires an exponent $\alpha < 1$. Solving Equation (67) by the separation of variables and integration yields,

$$m_{r,X}(t) = \left[m_{r,X,j}^{1-\alpha} - (1-\alpha) R_X \left(t - t_j\right)\right]^{\frac{1}{1-\alpha}} \quad ; \quad \text{with } R_X = \frac{\beta\left(GA_X \eta_X - \Delta C_{X\,j}\right)}{h_v m_{r0,X}^{\alpha}} \ . \tag{69}$$

Differentiation and using Equation (64) and multiplication by the enthalpy of vaporization results in the enthalpy flow of saturated steam from the region, *X* .

$$P_{v,X} = \dot{m}_{g,X} h_v = \frac{\rho_l - \rho_g}{\rho_l} R_X \left[m_{r,j}^{1-\alpha} - (1-\alpha) R_X \left(t - t_j\right)\right]^{\frac{\alpha}{1-\alpha}} \tag{70}$$

The total enthalpy flow from the collector array is,

$$P_v = \dot{m}_g h_v = n_C \left(P_{v,M} + P_{v,TH} + P_{v,BH}\right) \ . \tag{71}$$

Figure 8 shows the normalized enthalpy flow of steam in the isothermal case as a function of dimensionless time. The choice of $\alpha = 0.5$ is justified as follows.

For a short time interval of $\left(t_{j-1} - t_j\right) < 1\,\text{s}$, the second term within the square brackets of Equation (70) could be ignored because the magnitude of R_X is 10^3 times smaller than the initial residual mass. This would allow the differential equation for the steam propagation derived in the next section to be solved analytically and result in Equation (80). However, the choice of the exponent, α, is not critical, as will be explained in section 3.6. For $\alpha = 0.5$ Equation (70) is a linear function of time,

Preprints (www.preprints.org) | NOT PEER-REVIEWED | Posted: 30 December 2020 doi:10.20944/preprints202012.0750.v1

which allows to solve Equation (80) analytically for any time interval, as long as the saturation temperature can be considered as a constant. This is beneficial in two ways. In practical applications of this model, where the steam range is determined under constant but extremal conditions, the time interval can be considerably extended, which results in a short simulation time. Due to the analytical solution, no convergence issues occur.

3.5 *Steam propagation into the circuit*

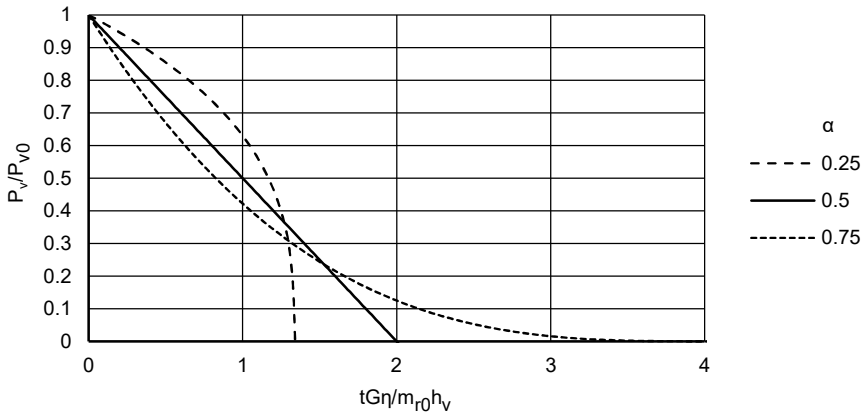

Figure 8 Relative enthalpy flow of steam as a function of dimensionless time.

Steam propagation into the circuit is described by the energy Equation (30), applied to a control volume defined by a finite section, k, of pipe. The index, k, is omitted where possible. Heat conduction in axial direction is ignored. A sharp phase boundary across the pipe cross-section is assumed. The flow across any pipe cross-section is therefore either steam or liquid. The liquid holdup, ε_l, of the steam-filled part of a pipe section is considered as zero. The void fraction of a pipe section is interpreted as the dimensionless location, x, of a virtual steam front.

$$\varepsilon = \frac{V_g}{V} = \frac{x}{l} \tag{72}$$

With these simplifications, the left-hand side of Equation (30) can be integrated and rearranged as follows:

$$\begin{aligned} &\frac{\partial}{\partial t}\iiint_{V_k}\left[\varepsilon\left(\rho_g u_g - \rho_l u_l\right) + \rho_l u_l\right]dV + \iint_{S_k}\varepsilon\left[\rho_g u_g \vec{w}_g - \rho_l u_l \vec{w}_l\right]d\vec{S} \\ &= A\dot{x}\left(\rho_g u_g - \rho_l u_l\right) + A\left(u_g \rho_g \vec{w}_g - u_l \rho_l \vec{w}_l\right) \end{aligned} \tag{73}$$

The first term of the right-hand side of Equation (30),

$$\sum \dot{Q} = -\dot{x} C_k \left(T_s - T_k\right) - x_k \cdot d_k \pi U_k \left(T_s - T_a\right) - x_k \frac{\partial}{\partial t}\left(C_k T_s\right), \tag{74}$$

consists of three parts. The first part describes the enthalpy flow into the pipe wall as it is exposed by the moving steam front. This term contributes only to positive velocities of the steam front. The second part accounts for the heat losses to the ambient. The third part describes the enthalpy flow due to change of saturation temperature. The time derivative of the enthalpy is replaced by the finite difference analogous to Equation (68). The heat capacity per unit length of a pipe section, C_k, depends on the specific heat capacities of the pipe and the steam.

$$C_k = A_w \rho_t c_t + A_t \rho_g c_g \tag{75}$$

The heat capacity of the insulating layer is ignored. The second term on the right-hand side of Equation (30) describes the rate of work exercised by the steam entering and the liquid leaving the control volume,

$$-\sum \dot{W} = -\iint_S p \vec{w} \vec{n} dS = A_k p\left(w_g - w_l\right) = p\frac{\dot{m}_{g,k}}{\rho_g} - p\frac{\dot{m}_{l,k}}{\rho_l} \tag{76}$$

Preprints (www.preprints.org) | NOT PEER-REVIEWED | Posted: 30 December 2020 doi:10.20944/preprints202012.0750.v1

Combining equations (73), (74) and (76), and substituting the phasic velocities by the mass flows $\dot{m} = A_t \rho w$ and the inner energies with enthalpies, $u = h - p/\rho$, leads to the following representation of the energy equation.

$$A_k \dot{x}\left(\rho_g u_g - \rho_l u_l\right) - \dot{m}_{g,k} h_g + \dot{m}_{l,k} h_l = -\dot{x} C_{t,k}\left(T_s - T_k\right) - x \cdot d_k \pi k_k \left(T_s - T_a\right) - x \Delta C_k \tag{77}$$

From the mass conservation applied to the same control volume one gets a formula for the liquid mass flow across the boundary.

$$\dot{m}_{l,k} = \dot{m}_{g,k} - \dot{x} A_k \left(\rho_g - \rho_l\right) \tag{78}$$

Substituting into Equation (77) and replacing the enthalpies of saturated steam and water with the enthalpy of vaporization, h_v, results in a differential equation for the location, x, of the steam front within the control volume defined by the pipe section, k.

$$\dot{x}\left[A_k \rho_g h_v + C_k\left(T_s - T_k\right)\right] + x\left[d_k \pi U_k \left(T_s - T_a\right) - \Delta C_k\right] = \dot{m}_{g,k} h_v \tag{79}$$

The enthalpy flow, $\dot{m}_{g,k} h_v$, of saturated steam entering the pipe section, k, is equal to the enthalpy flow of steam leaving the collector, $P_v = \dot{m}_g h_v$, with the mass flow of steam from Equation (71), reduced by the heat flux, c, dissipated from the steam into the pipe walls.

$$\dot{m}_{g,k} h_v = P_v - c = \dot{m}_g h_v - c \tag{80}$$

Inserting this equation into Equation (79) and substituting Equation (71) for the steam power results in a differential equation for the location, x, of the steam front.

$$\dot{x} a + x b = e - f\left(t - t_j\right) - c \tag{81}$$

The quantities, e, and, f, are defined for the whole collector array consisting of n_C collectors and regions $X \in \{Ht, M, Hb\}$ as follows:

$$e = \frac{\rho_l - \rho_g}{\rho_l} n_C \beta G \sum_X \left[\left(A_X \eta_X - \Delta C_{X,j}\right)\left(\frac{m_{r,X}}{m_{r0,X}}\right)^{1/2}\right] \tag{82}$$

$$f = \frac{\rho_l - \rho_g}{\rho_l} \frac{n_C \beta^2}{2 h_v} \sum_X \left[\frac{\left(G A_X \eta_X - \Delta C_{X,j}\right)^2}{m_{r0,X}^{1/2}}\right] \tag{83}$$

Since the pressure losses and the influence of check valves are ignored, the height levels of the steam front in the supply- and return lines are identical. If the phase boundaries of both the supply and return line are located in horizontal pipe sections, both steam fronts are assumed to propagate at the same speed. These rules are formally implemented by parameters, $\delta_k = 0,1$ and $\delta_q = 0,1$, according to Table 1 and the coefficients, a, b and c, defined as follows:

$$\begin{aligned} a &= \delta_k \left[A_k \rho_g h_v + C_k\left(T_s - T_k\right)\right] + \delta_q \left[A_q \rho_g h_v + C_q\left(T_s - T_q\right)\right] \\ b &= d_k \pi U_k \left(T_s - T_a\right) + \Delta C_k + d_q \pi U_q \left(T_s - T_a\right) + \Delta C_q \\ c &= \sum_{i=1}^{k-1} l_i \left[d_i \pi U_i \left(T_s - T_a\right) + \Delta C_i\right] + \sum_{i=1}^{q-1} l_i \left[d_i \pi U_i \left(T_s - T_a\right) + \Delta C_i\right] \end{aligned} \tag{84}$$

Table 1 Propagation parameters and pipe direction with respect to the inlet and outlet of the collector field.

Supply line	Return line	δ_k	δ_q
horizontal	horizontal	1	1
horizontal	downward	1	0
downward	horizontal	0	1
downward	downward	1	1

An increase in steam volume usually accompanies an increase in pressure. Therefore, all coefficients become time-dependent. However, within a sufficiently short time step the coefficients can be

Preprints (www.preprints.org) | NOT PEER-REVIEWED | Posted: 30 December 2020 doi:10.20944/preprints202012.0750.v1

considered as constant, which allows the derivation of an analytical solution. The solution of the homogeneous part of Equation(81) is,

$$x_h = C_1 \exp\left[-\frac{b}{a}\left(t - t_j\right)\right] \quad , \tag{85}$$

The solution of the inhomogeneous equation has the form,

$$x_p = C_2 + C_3\left(t - t_j\right). \tag{86}$$

Comparing of coefficients yields,

$$C_2 = \frac{1}{b}\left(e - c + \frac{fa}{b}\right) \quad ; \quad C_3 = -\frac{f}{b} \tag{87}$$

Inserting the initial condition, $x_h\left(t_j\right) + x_p\left(t_j\right) = x_j$, yields the constant, C_1, of the homogeneous solution.

$$C_1 = x_j - C_2 \tag{88}$$

Finally, the location of the steam front, starting at the initial time, t_j, is,

$$x\left(t - t_j\right) = \left(x_j - \frac{P_v - c}{b}\right)\exp\left[-\frac{b}{a}\left(t - t_j\right)\right] + \frac{P_v - c}{b} \quad . \tag{89}$$

Of interest are also the heat losses from the pipes to the ambient, $\dot{Q}_{loss}$, and the total dissipated heat from the steam to the pipes, $\dot{Q}_{diss}$, which are calculated using Equation(84).

$$\dot{Q}_{diss}\left(x_k, x_q\right) = c + x_k\left[d_k \pi U_k\left(T_s - T_a\right) + \Delta C_k\right] + x_q\left[d_q \pi U_q\left(T_s - T_a\right) + \Delta C_q\right] \tag{90}$$

$$\dot{Q}_{loss}\left(x_k, x_q\right) = \left[\sum_{i=1}^{k-1} l_i d_i \pi U_i + l_k d_k \pi U_k + \sum_{i=1}^{q-1} l_i d_i \pi U_i + l_q d_q \pi U_q\right]\left(T_s - T_a\right) \tag{91}$$

The change rate of heat, $\dot{Q}_{accum}$, accumulated by the steam filled parts of the collectors is,

$$\dot{Q}_{acc} = \beta \sum_X \Delta C_X \left(\frac{m_{r,X}}{m_{r0,X}}\right)^{\alpha} \tag{92}$$

3.6 *Numerical procedure*

The equations describing the states of the MEV, the steam-filled parts of the circuit and the absorber regions are formally coupled by shared state variables. Therefore incremental calculation can lead to oscillations of these variables. Some of these oscillations, like the pressure transients observed in reality [7, p.67], are caused by the physical processes. Others, which could be limited by a sufficiently short time step, are caused by the numerical procedure. A time step of 0.2 seconds proved to be a good compromise between computing time and time resolution. Inexplicable peaks and oscillations are sufficiently canceled out by taking the average of new and previous values of pressure, saturation temperature and the change rates of heat, where the previous values are weighted by a factor of 20. The consequently resulting infringement of the law of conservation of energy is negligible.

The residual mass of the system with standard selective absorbers is calculated based on a 5 min average of solar irradiation. For the system with thermochromic absorbers the solar irradiation is averaged over 10 min. The starting point of the time series is taken as the moment when saturation conditions are reached.

Preprints (www.preprints.org) | NOT PEER-REVIEWED | Posted: 30 December 2020 doi:10.20944/preprints202012.0750.v1

Eleven experimental data sets for both solar thermal systems were available. According to the properties of the model only four data sets from experiments with inactive check valves were used for model calibration. The unknown parameters were determined iteratively by a qualitative procedure displayed in Figure 9.

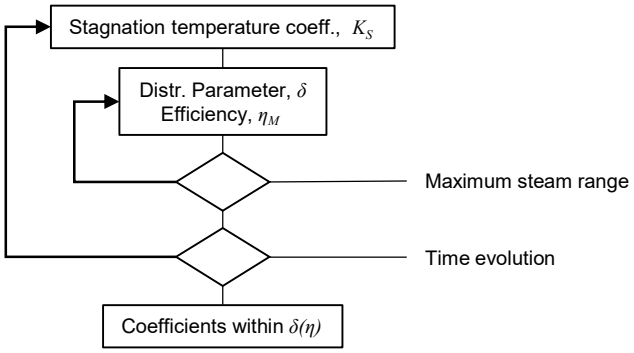

Figure 9 Procedure to determine model parameters.

An initial value for the parameter, K_S, for the effective stagnation temperature in Equation (2), was chosen. The distribution parameter, δ, was varied until the measured and simulated steam ranges matched. The corresponding efficiency of the meander region, η_M, was stored for curve fitting. The time evolutions of the measured and simulated steam ranges were compared. If the gradients of the simulated steam range, which depend on the efficiency, were too small, the value of the parameter, K_S, was increased and vice versa. This procedure was repeated until the steam ranges and the time evolutions matched. Finally the parameters of the distribution function, Equation (49), were determined, based on the final values $\delta(\eta_M)$.

4 Results and discussion

The initial states of the two solar thermal systems were determined by running in normal operation prior to pump shutdown. The pumps of both systems were switched off manually at the same time. The subsequent process of stagnation is discussed in the following sections as a comparison between measured and simulated data.

4.1 Comparison of experimental data and simulations

Both solar thermal systems were simulated using the initial and boundary conditions from data sets of eleven experiments. Figure 10 shows measured and simulated total maximum steam ranges, i.e. the total steam ranges in the supply and return line. The confidence limits are based on the assessment of uncertainties in section 4.2.

In seven experiments, the check valves were active (transparent markers). As a result, a height difference of the liquid columns within the return- and supply line establishes, which roughly corresponds to the opening pressure of two serial check valves. As soon as the steam range reduces, the circuit is refilled via the return line. If the solar gain and/or released heat from the tube walls are sufficient to vaporize the entering liquid, the steam volume within the collector and the steam range in the supply line are maintained beyond the time span considered.

In four experiments, the check valves were manually opened after pump shutdown (filled-out markers). As expected, the steam ranges in the system with thermochromic absorbers (red markers) are considerably smaller than in the system with conventional selective absorbers (black markers). A higher system pressure, based on a preset overpressure of 2 bar, also leads to smaller steam ranges (rhombic markers) than with a system overpressure of only 1 bar (circles), based on a preset pressure of 1 bar. The circles marked with a white cross correspond to the dataset “08-16” which was used to determine the uncertainties in section 4.2. The circle marked with a star corresponds to the dataset “07-25” which is discussed in Figure 15.

Preprints (www.preprints.org) | NOT PEER-REVIEWED | Posted: 30 December 2020 doi:10.20944/preprints202012.0750.v1

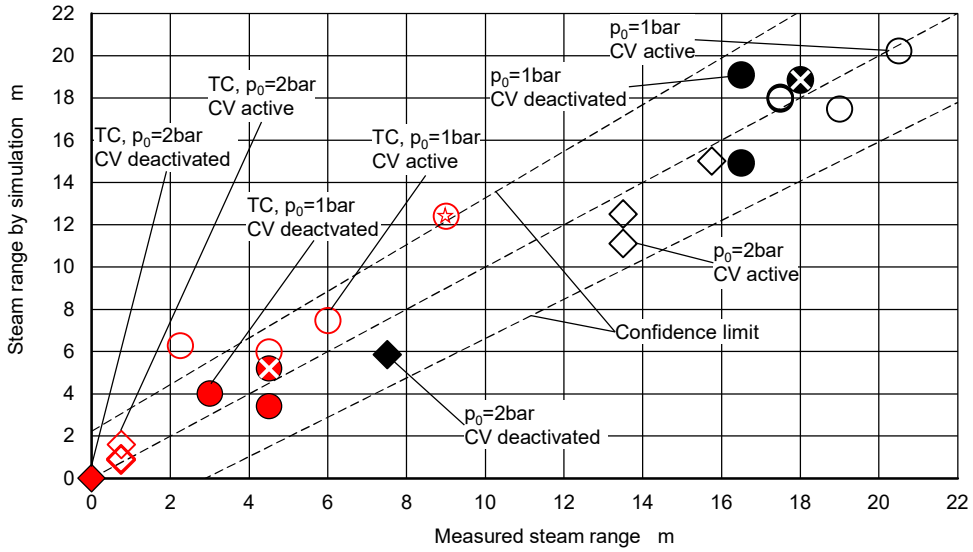

Figure 10 Comparison of total steam ranges from experimental data and simulations for the system with thermochromic absorbers (red) and conventional selective absorbers (black).

The numerical data are listed in Table 2, together with the measured solar irradiance and the residual mass of the water-glycol mixture. The averaged irradiance data listed in Table 2 differ for two reasons. The system with thermochromic absorbers (TC) reaches the onset of evaporation later than the system with standard selective absorbers (SC). The averages are taken over the approximate period, τ , of liquid displacement, which was estimated as τ_{SC} = 300s, and τ_{TC} = 600s.

Table 2 Average irradiation on the system with the standard selective (SC) and thermochromic (TC) absorber coating. Experimental and simulation results of the total steam range and simulation results of the residual mass. Active check valves (CV) are indicated by "✓".

Dataset	CV	p_0	<G>		Residual mass		Total steam range			
mm-dd	-	bar	W/m²	W/m²	kg	kg	m		m	
			SC	TC	SC	TC	SC	TC	SC	TC
			Exp.	Exp.	Sim.	Sim.	Exp.	Exp.	Sim.	Sim.
07-24	✓	1	960	960	1.61	2.24	19.0	4.5	17.5	6.0
07-25	✓	1	1014	1014	1.52	1.74	20.5	9.0	20.2	12.4
07-26	✓	1	960	956	1.60	2.16	17.5	2.3	18.0	6.3
07-27	✓	1	902	903	1.63	2.17	20.5	6.540	19.6	7.5
08-02	✓	2	960	960	2.03	6.59	13.5	0.8	11.1	0.9
08-03	✓	2	988	988	1.78	3.72	15.8	0.8	15.0	1.6
08-06	✓	2	997	997	1.89	5.15	13.5	0.8	12.5	0.9
08-16	-	1	986	990	1.59	2.40	18.0	4.5	18.9	5.2
09-04	-	1	892	890	1.82	6.90	16.5	4.5	14.9	3.4
09-05	-	1	948	950	1.61	2.70	16.5	3.0	19.1	4.0
09-18	-	2	948	948	2.39	6.83	7.5	0.0	5.9	0.0

The comparison of experimental and simulated data shown in Figure 10 and Table 2 leads to the following conclusions.

- For the system with standard selective absorbers, the simulated values for the total steam ranges lie well within the confidence limits. No significant difference between active and open check valves can be determined. It follows that the effect of the check valves on displacement and evaporation processes within the collector array is negligible.

Preprints (www.preprints.org) | NOT PEER-REVIEWED | Posted: 30 December 2020 doi:10.20944/preprints202012.0750.v1

- For the system with thermochromic absorbers, the steam ranges with open check valves are within the confidence range, whereas the model tends to overestimate steam ranges in the cases with active check valves.

It should be noted that information on the total steam range is not sufficient. In the next sections the considerable effect of the check valves on the individual steam ranges in the supply and return lines will be discussed.

4.1.1 Conventional selective absorbers, deactivated check valves

Figure 12 a) shows the steam range within the supply and return lines of the system with conventional selective absorbers for the dataset 08-16. The check valves were manually opened at the same time as the pump was switched off. The experimental data are interpreted as follows. About 13 minutes after pump shutdown, steam starts to leave the collector and first enters the supply line, as expected. Even before the steam front reaches level the lower header, steam enters the return line. A small hydrostatic imbalance is established, which is compensated by pressure losses within the collector array. Between 21 and 25 min after pump shutdown the steam range is maximal in both the supply- and return line.

In the simulation, at about the same time as in the experiment, the beginning vaporization causes steam to enter the supply line. The continuous black line shows the corresponding height of the liquid level. As soon as the steam reaches the level of the lower header (dashed black line) the steam expands also into the return line. Because the model does not account for pressure losses, the liquid levels are the same and the continuous and dashed black lines overlap. The simulated steam range reaches a maximum 24 min after pump shutdown, which coincides quite well with the experiment. Figure 11

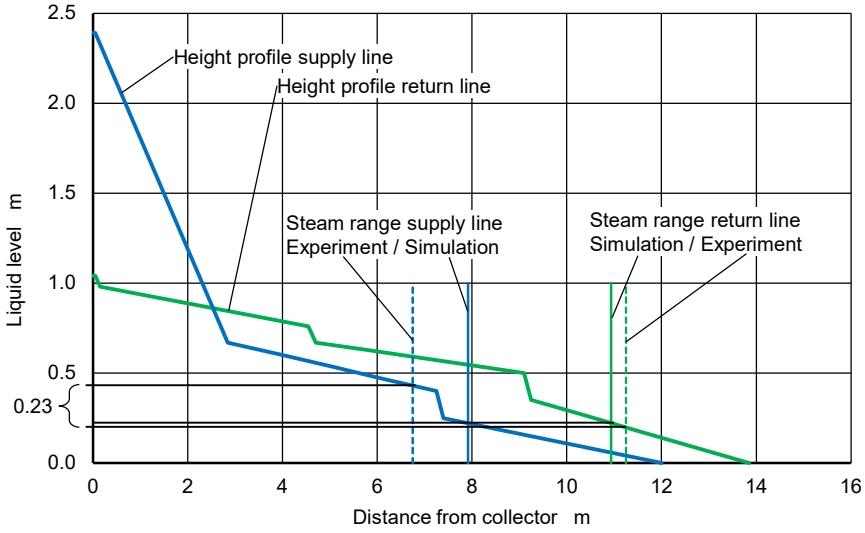

Figure 11 Height profiles of the supply and return lines.

shows the height profiles and the maximal steam ranges of the supply and return lines. In the experiment, the liquid levels differ by 0.23 m. This is very little and justifies the assumption that the pressure losses can be neglected. Consequently, the liquid levels in the simulation are equal.

Preprints (www.preprints.org) | NOT PEER-REVIEWED | Posted: 30 December 2020 doi:10.20944/preprints202012.0750.v1

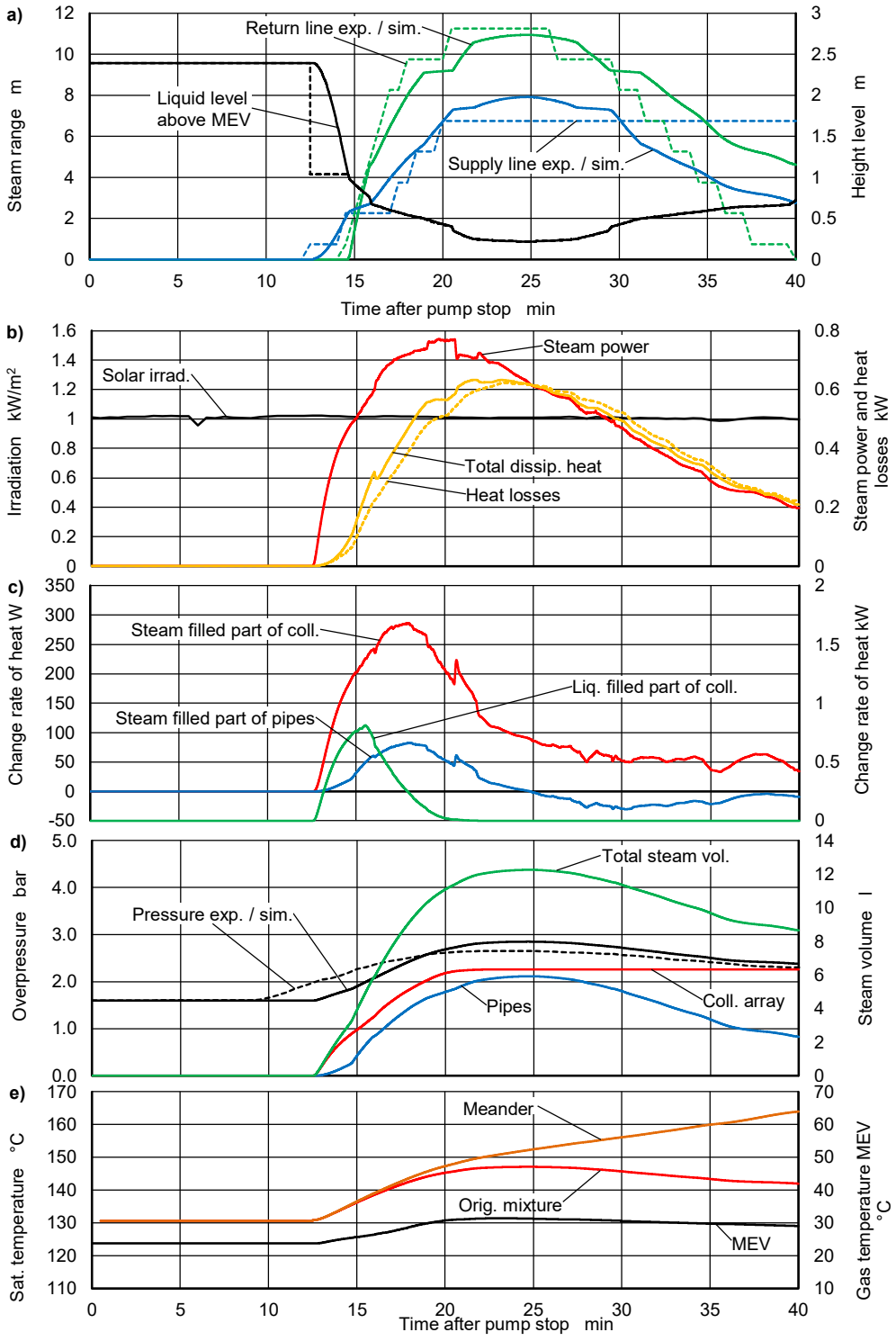

Figure 12 Experimental and simulation results for the system with Standard selective absorbers. Opened check valves. Case 08-16.

Up to 30 minutes after pump shutdown, the simulated results are close to the experimental values. After that, the simulation results for the supply line decrease, whereas in the experiment the steam stays constant within the considered time span. There are two main reasons for the deviation of the simulation from the experiment. 1) From the beginning of the vaporization process, steam leaving the meander tube penetrates a layer of residual liquid in the upper header. If the velocity of

Preprints (www.preprints.org) | NOT PEER-REVIEWED | Posted: 30 December 2020 doi:10.20944/preprints202012.0750.v1

the steam drops below a certain value, gravity starts to dominate the interfacial friction and liquid trickles into the meander tube where it vaporizes within a short distance from the junction. Due to the albeit small pressure losses, the steam created by this process leaves the collector array mainly by the upper connection and enters the supply line, thereby maintaining the steam range for a longer time. 2) The increasing concentration of glycol leads to an increasing concentration of the glycol content in the vapor phase, which is not reflected by the model.

Figure 12 b) shows the simulated steam power, the heat losses and the thermal power dissipated into the steam- filled parts of the supply and return lines. The difference between steam power and dissipated thermal power corresponds to the heating-up of the pipe walls from their initial temperature to saturation temperature as the steam front propagates. The difference is quite high because the initial temperatures of the supply and return lines are only 49 °C and 38 °C. Since the pressure and the saturation temperature increase while the steam range increases (see Figure 12 d and e), the heat flow dissipated into the pipes is higher than the heat losses into the ambient. The difference is accumulated in the pipes. The steam range increases until the heat losses, the dissipated heat flow, and the steam power coincide.

Figure 12 c) shows the simulated enthalpy change of the liquid-filled part of the collector during heating-up, which becomes zero as soon as the liquid mass flow displaced from the collector array into the supply and return lines becomes zero. Also shown is the enthalpy change of the steam-filled regions of the collector field and the pipes due to pressure change. If the pressure and thus the saturation temperature increase, the steam-filled parts of the pipes accumulate heat. With decreasing steam range, the pressure decreases, too, and heat is released again. In the collectors, however, the saturation temperature of the residual liquid increases because the water content of the mixture decreases. Therefore, in this case, the enthalpy change rate is always positive. This can also be concluded from the monotonic growth of the saturation temperature of the residual liquid shown in Figure 12 e). Also shown in the same figure is the temperature course of the gas volume within the MEV.

It is essential to take the heat capacities of the pipe walls and the collectors into account. Otherwise, a much faster process and a considerably higher steam range would result. The following effect is also caused by heat capacity and the pressure transient. About 22 min after pump stop the steam front leaves the long, slightly downwardly-sloped pipe section and enters the short, nearly vertical connector that leads to the next long, downwardly-sloped pipe section. This is visible by the sudden decrease in level height in Figure 12 a). As a result, pressure and saturation temperature also increase, which causes the heat transfer rate into the steam-filled parts of the collectors and pipes to increase as well. This is indicated by the sudden increase in the dissipated heat flow into the pipes visible in the corresponding curves in Figure 12 b) and Figure 12 c) and the sharp decrease in the steam power in Figure 12 b).

Figure 12 d) shows the pressure transients and the development of steam volume in the collector field and the pipes. The pressure depends only on the state of the MEV, i.e. the liquid volume transferred from the circuit into the MEV by the growing steam volume, on the temperature of the gas volume and on the height of the liquid column above the MEV.

4.1.2 Conventional selective absorbers, check valves active

The check valves are of the spring-loaded type, which require a pressure of 0.04 bar to open in flow-direction. Therefore, a corresponding difference of liquid levels occurs and the steam displaces the liquid mainly via the return pipe into the MEV.

Figure 13 a) shows the steam ranges from simulation and experiment for the dataset 07-26. The experimental results show the expected asymmetry. A height difference of about 1 m is established, which corresponds to the head loss of two serially-connected check valves. The model does not reflect this effect. The fact that the total steam range from the simulation nevertheless corresponds closely to the experimental value can be explained as follows: During the early stages of liquid displacement,

Preprints (www.preprints.org) | NOT PEER-REVIEWED | Posted: 30 December 2020 doi:10.20944/preprints202012.0750.v1

the two-phase pressure loss within the collector array causes a pressure difference across the check valves in normal flow direction. Apparently, the pressure difference is higher than the opening pressure of the check valves. As a result, the displacement process is basically the same as in the case with open check valves. This is confirmed by the fact that, at the very beginning of steam expanding into the circuit, steam enters the supply line first.

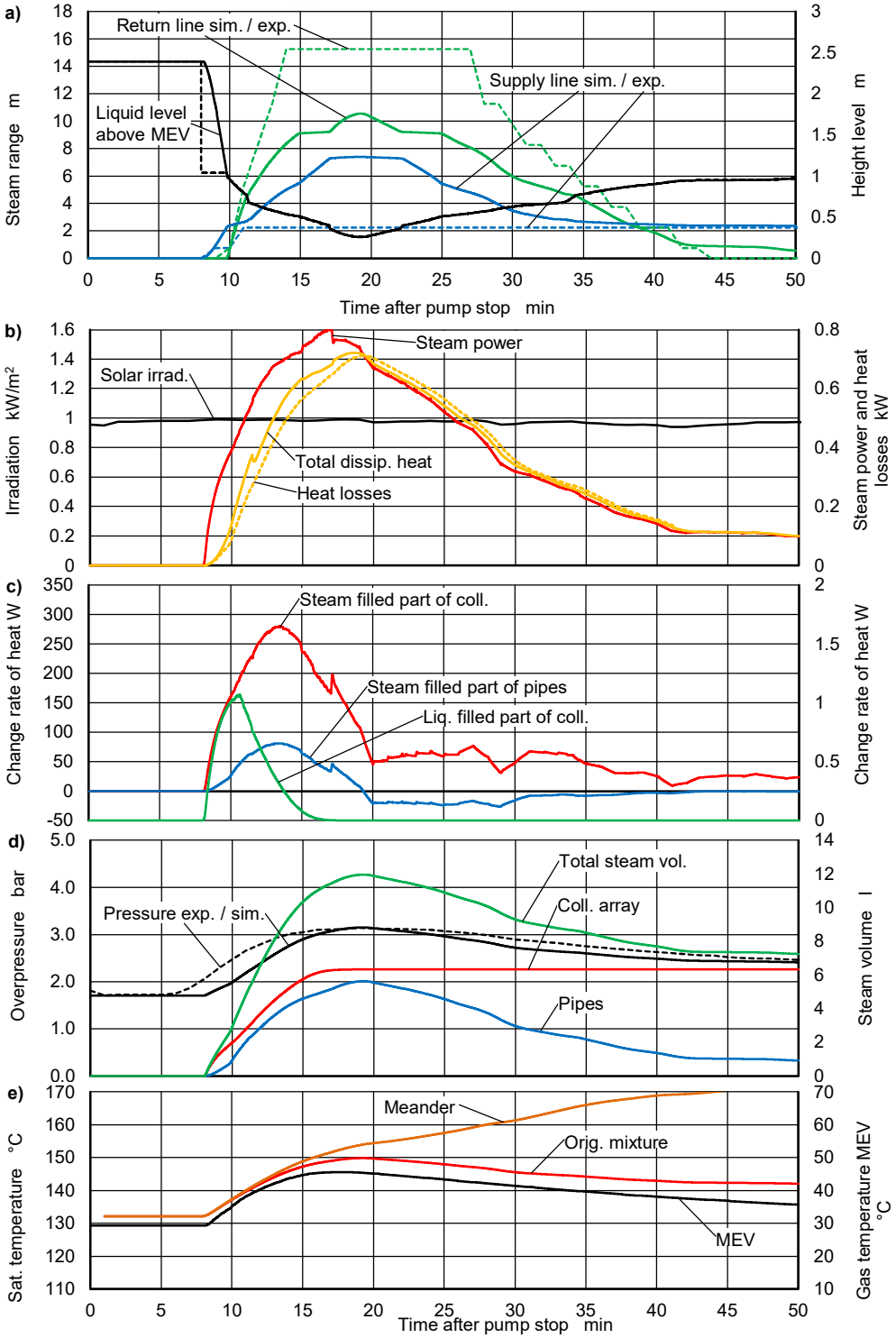

Figure 13 Experimental and simulation results for the system with Standard selective absorbers. Active check valves. Dataset 07-26.

Preprints (www.preprints.org) | NOT PEER-REVIEWED | Posted: 30 December 2020 doi:10.20944/preprints202012.0750.v1

In later stages of stagnation, the pressure loss is much smaller than the opening pressure of the check valves, which results in the different steam ranges as can be seen in the experimental values.

The initial pipe temperatures of the supply and return lines immediately before pump stop are 94°C and 88°C for the dataset 07-26 compared to only 49 °C and 38 °C for the dataset 08-16. There is less steam power needed to heat the pipe walls up to saturation temperature. Furthermore, the average solar irradiation for the dataset 07-26 is about 3% higher than for 08-16. Based on these data alone one would expect a significantly higher total steam range for 07-26. However, the total steam ranges are practically the same. This is explained by the following countering effect. Because of liquid expansion due to the higher circuit temperature the initial pressure in the case 07-27, Figure 13 d) is about 0.2 bar higher than the initial pressure for 08-16, Figure 12 d). Consequently, the saturation temperature is higher, which results in a lower collector efficiency. In this example, the steam range is practically independent from the initial temperature. However, with a larger MEV or even a compressor type of pressure maintenance system, where the pressure is kept within the range of a small hysteresis, the maximum steam range would increase with increasing initial temperature. This must be kept in mind when designing a solar thermal system.

4.1.3 Thermochromic absorbers – deactivated check valves

Figure 14 a) shows the development of the steam range in the system with thermochromic absorbers for the dataset 08-16. The steam ranges are slightly overestimated, but the time evolution is qualitatively consistent. As expected, steam enters in the supply line first. In the experiment, the steam range in the return line starts to develop about 5 min later than in the simulation, which is interpreted as follows: Due to the lower efficiency, the vaporization rate is lower than with standard selective absorbers. As a result, interfacial friction is so weak that liquid within the pipe bends flows downwards against the steam flow. This results in a more pronounced separation of the steam region, which occupies the top of the meander, from the liquid filled region below. In consequence, the liquid is almost entirely displaced into the return line. This process is mainly balanced by the pressure losses within the meander tube which leads to a corresponding difference of the liquid levels. Compared to the system with standard selective absorbers, where a symmetrical steam flow distribution is a reasonable assumption, the origin of evaporation lies at a location much closer to the top of the meander. In consequence, a larger proportion of the residual mass accumulates in the lower regions of the absorber and, driven by gravity and the weak interfacial friction exercised by the co-current steam flow, enters the lower header and finally the return line. Figure 14 b) shows the corresponding steam power and pipe heat losses.

4.1.4 Thermochromic absorbers – active check valves

In the experiments where the check valves are active, this effect is even more pronounced. The liquid is almost completely displaced into the return pipe. Due to the imbalance caused by the opening pressure of the check valves, the steam generally flows downwards driving the residual liquid towards the lower regions. As a result, the total steam range is lower compared to situations where the check valves are open, which corresponds to the results of dedicated experiments on a solar system with the same hydraulic design [2]. This is the reason why the steam ranges for collectors with thermochromic absorbers and operational check valves, datasets 07-24 to 07-27, are generally overestimated by the model, as displayed in Figure 10 (red circles). The effect is much less pronounced for the datasets 08-03, 08-04 and 08-06, where the collector efficiency is very low.

Preprints (www.preprints.org) | NOT PEER-REVIEWED | Posted: 30 December 2020 doi:10.20944/preprints202012.0750.v1

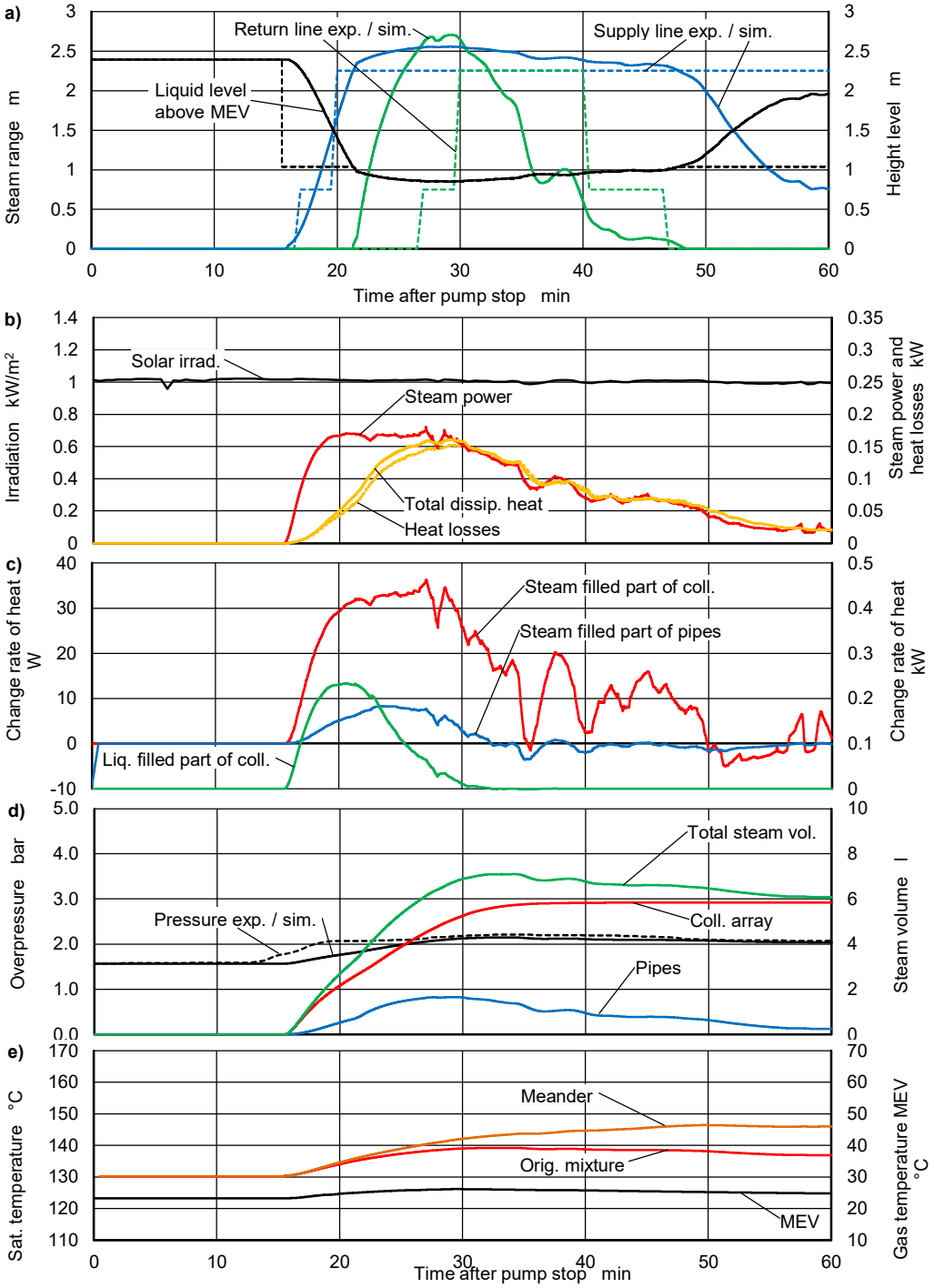

Figure 14 Experimental and simulation results for the system with thermochromic absorbers. Inactive check valves. Dataset 08-16.

As can be seen in Figure 15, the simulation not only considerably overpredicts the total maximum steam range. In addition, the progressions of experimental and simulated steam ranges do not even correspond qualitatively.

Preprints (www.preprints.org) | NOT PEER-REVIEWED | Posted: 30 December 2020 doi:10.20944/preprints202012.0750.v1

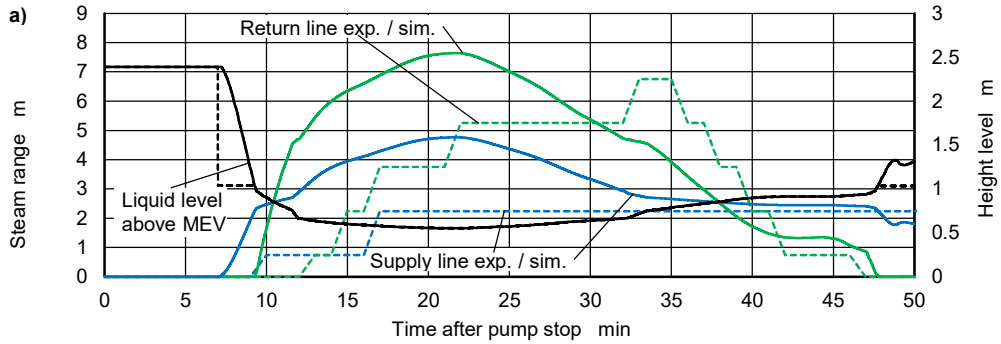

Figure 15 Steam range from experiment and simulation for the system with thermochromic absorbers. Active check valves. Dataset 07-25.

4.2 *Uncertainties*

The distance between the temperature sensors are $\Delta x = 1.5\,\mathrm{m}$ in both the feed- and the return line. According to Scheuren [11], the uncertainty of the steam front location due to the equidistant location of sensors can be determined using the relation of Kirkup and Frenkel [32]:

$$\sigma_{\Delta x} = \Delta x / \sqrt{3} = 0.87\,\mathrm{m} \tag{93}$$

Due to the small slope angle, φ, of the long pipe sections the phase boundary occupies about $\sin(\varphi) d_t \approx 0.5\,m$ of pipe length. Within this region, the average temperature of both the liquid and the pipe are below saturation as the steam range increases. Furthermore, the high conductivity of the copper tubes prevents sharp changes of temperature. These effects add about $\sigma_\varphi = 0.25\,\mathrm{m}$ to the uncertainty in the steam range.

The uncertainties of boundary conditions and material properties and their effect on the steam range was determined by simulation based on the dataset 08-16. According to Kovacs [33], an uncertainty of 2% for the measured solar irradiance and an uncertainty of 4% for the collector efficiency at saturation conditions are assumed. The uncertainty of the preset pressure of the MEV depends on the uncertainty of the pressure gauge readings of 0.05 bar. Assuming an uncertainty of the gas temperature within the MEV of 10K at the time of setting the preset pressure results in a further uncertainty of about 0.05 bar. The uncertainty of the heat conductivity of the pipe insulation was estimated at 10 %. The uncertainty of local ambient temperature and the wind velocity are not considered. The uncertainties and their effect on the steam range are listed in Table 3.

Table 3 Uncertainties of material properties and boundary conditions and their effect on the simulated steam range, based on data set 08-06.

Quantity	uncertainty	Effect on steam range m	
		Standard	Thermochromic
Solar irradiance	±2%	+1.06/-1.01	+0.87/-0.90
Collector efficiency	±4%	+0.49/-0.49	+0.17/-0.28
Preset gauge pressure 1bar	±0.1 bar	+0.46/-0.51	+0.22/-0.34
Heat conductivity of pipe insulation	±10%	-0.8/+0.96	-0.3/+0.32

Based on these results, a total average uncertainty of ± 4 m for the system with standard selective absorbers and ± 2.9 m for the system with thermochromic absorbers was determined?). When simulating the steam range during system dimensioning, an increase the simulated steam ranges by the relative uncertainties listed in Table 4 is suggested.

Preprints (www.preprints.org) | NOT PEER-REVIEWED | Posted: 30 December 2020 doi:10.20944/preprints202012.0750.v1

Table 4 Relative uncertainty to be used in system dimensioning.

	Steam range m	Average uncertainty m	Relative uncertainty -
Selective absorbers	18	4.0	0.22
Thermochromic absorbers	4.5	2.9	0.63

For two reasons, application of the drift flux model poses the most fundamental uncertainty of the model. On the one hand, this correlation was neither validated nor intended to be used at the limit of vanishing liquid mass flow. On the other hand, it is only strictly applicable for constant superficial velocities in straight pipes. However, for absorber tubes with diameters equal to or smaller than 9 mm the error is sufficiently low. For larger pipe diameters, flow-pattern independent drift-flux correlations [34,35] or a combination with flooding correlations might be better suited.
A more detailed analysis of uncertainties is not possible because the number of data sets and the number of quantities affected by uncertainties are of the same magnitude.

5. Conclusions

A transient model for the stagnation of solar thermal systems was derived based on the integral form of a two-phase mixture model. Based on scientific articles and the author's own experience that fast pressure transients with large amplitudes do not occur, the momentum conservation equation was replaced with a simple pressure balance and a drift flux model. With successive simplifications it was possible to derive at a one-dimensional representation of the mixture model. The resulting differential equation for the steam range could be analytically integrated over short time periods. Thus, stability problems were avoided, and efficient computing was achieved.

The fact that displacement and steam generation occur at the same time has been considered by defining two time-dependent volume fractions, one completely liquid-filled, the other containing steam and residual liquid. Steam generation within the liquid-filled volume fraction is attributed to liquid displacement whereas evaporation of the residual mass is linked to steam generation. This made it possible to formulate liquid displacement and steam expansion into the circuit by two sets of energy and mass conservation equations. Heat losses from collectors and pipes to the ambient are modelled by well-established correlations for convective and radiative heat transfer. A transient model for the gas temperature inside the membrane expansion vessel was also derived. The model leaves only four parameters unknown, which were determined by comparison of experimental and simulated data. One parameter, in Equation (2), accounts for the fact that the effective stagnation temperature of a collector lies between the temperature of dry stagnation and the temperature where the solar gain at normal operating conditions is zero. The three other parameters are part of a correlation, Equation (49) for the ratio of residual mass relevant for steam expansion into the circuit, to the residual mass calculated by the drift flux model, which is valid only for stationary conditions. The model is applicable to solar systems with flat-plate collectors and meander-type absorbers with tube diameters ≤ 9 mm. Application to other hydraulic concepts and larger diameters of absorber tube requires different correlations for the residual mass and calibration experiments with collectors of the particular hydraulic concept.

In order to calibrate the model, an experimental facility was designed and built, dedicated to the performance of well-defined stagnation tests under real conditions. The facility consists of two solar thermal systems, the one with standard selective absorbers, the other with thermochromic absorbers. Two spring-loaded check valves prevent natural circulation in the circuit and protect the pump from hot liquid and/or steam during stagnation. Experiments with active and deactivated check valves were carried out. Since the model does not account for the effects of the check valves, only experiments with deactivated check valves were used to determine the unknown parameters.

In the experiments where the check valves were deactivated, i.e. opened immediately after pump shutdown, the experimental values of the liquid levels in the supply and return lines where almost equal. Therefore the simulated progression of the steam ranges in the supply- and return lines correspond well to the experimental values.

Preprints (www.preprints.org) | NOT PEER-REVIEWED | Posted: 30 December 2020 doi:10.20944/preprints202012.0750.v1

The experiments with active check valves show a distinct difference of the liquid levels due to the opening pressure of the check valves. The simulation result of the system with standard selective absorbers correspond well to data from experiments with active as well as deactivated check valves. Thus, check valves have practically no effect on the total steam range. It can be concluded that the magnitude of the pressure losses within the meander tube is larger than the opening pressure of the check valves.

The simulation results of the system with thermochromic absorbers correspond well to data from experiments with deactivated check valves. With activated check valves, both the progression of the steam range and its total maximum differ considerably. Due to the much lower velocities of steam and liquid in the system with thermochromic absorbers, the associated pressure losses are lower than the opening pressure of the check valves. Therefore, phase separation is more pronounced, and a larger amount of liquid is displaced via the return line, resulting in a smaller amount of residual liquid and, in consequence, a smaller steam range. Since the model does not account for the effects of the check valves, the simulation tends to overestimate the steam range.

It is important to note that the effect of the check valves must be considered when dimensioning a solar system. It is suggested that the steam range in the supply- and return line should be corrected in accordance to Equations (94), which are functions of the inclination angle and the number, n, of the check valves and their opening pressure, Δp .

$$\Delta l_{v,SL} = \frac{n\Delta p}{2\rho g \sin(\varphi)} \quad ; \quad \Delta l_{v,RL} = -\frac{n\Delta p}{2\rho g \sin(\varphi)} \tag{94}$$

In general, the model is capable of predicting the maximum steam range well within the accuracy needed for system design. Due to the complexity of the experimental facility, which represents two real systems, as well as the transient ambient conditions and the limited number of sensors, it is not possible accurately to attribute experimental data to certain effects.

The model is implemented into the open-source simulation tool THD, dedicated to the thermal-hydraulic dimensioning of solar systems up to about 100 m² collector area [17,36]. The actual size is limited mainly by the validity of the assumption that pressure losses during stagnation are negligible. Tools of this kind will become increasingly important as the key to designing both cost effective and operationally safe solar systems.

Supplementary Materials: The software tool is available at https://sourceforge.net/projects/thd/

Author Contributions: Derivation of the model and programming, Eismann Ralph; concept and design of the experimental facility, Giovannetti Federico and Hummel Sebastian; building, instrumentation and calibration of the experimental facility, Hummel Sebastian; experimental work including data acquisition and post-processing, Hummel Sebastian; writing—original draft preparation, Eismann Ralph.; writing—review and editing, Giovannetti Federico and Hummel Sebastian.

Acknowledgements: This research was funded partially by the Swiss Federal Office of Energy, grant number SI/501722-01, and by funds from the research program Future Energy Efficient Buildings and Districts (FEEB&D) of the Swiss Competence Center for Energy Research (SCCER), grant number CTI.2014.0119. The experimental part was carried out in the frame of the project "Process technology, quality assessment and system solutions for thermochromic absorbers in solar thermal collectors (ProTASK)", which was funded by the German Federal Ministry of Economic Affairs and Energy based on a decision of the German Federal Parliament (reference numbers 0325858 A and B). The authors would like to thank Nick Moon and Peter Fry for proofreading.

Preprints (www.preprints.org) | NOT PEER-REVIEWED | Posted: 30 December 2020 doi:10.20944/preprints202012.0750.v1

Appendix A

The coefficients of the collector model, equation (1), and the heat capacities of the meander- and header regions in dry state are listed in **Table 5**.

Table 5 model characteristics of collectors

Quantity	Unit	Standard	Thermochromic	
Critical temperature Tc	°C	-	68	
Temperature range			$T \le T_c$	$T > T_c$
zero-loss efficiency factor	-	$\eta_0 = 0.785$	$\eta_0 = 0.757$	$\eta_{0,TC} = 0.83$
Heat loss coefficient	W/Km²	$a_1 = 4.19$	$a_1 = 4.27$	$a_{1,TC} = 6.17$
Heat loss coefficient	W/K²m²	$a_2 = 0.0135$	$a_2 = 0.0065$	$a_{2,TC} = 0.0103$
Stagnation temperature	°C	192.1	167	
Dry meander region heat capacity	J/K	2793		
Meander volume	l	0.924		
Dry header region heat capacity	J/K	566		
Header volume	l	0.660		
Aperture area	m²	2.33		
Hydraulic elements	Length m	d_i m	Number of nodes -	
Absorber tube	21.88	0.0082	88	
Header tube	1.1	0.02	1	

The material properties of the insulation layer are shown in **Table 6**. The optical properties have been estimated. The heat conductivity is modelled by a 2nd order polynomic based on the data-sheet [21],

$$\lambda = \lambda_0 + a\vartheta + b\vartheta^2 . \quad (95)$$

Table 6 Material properties of the pipe insulation

Heat conductivity	W/Km	W/°C²m	W/°C³m
	0.03764	7.70E-05	8.00E-07
Absorption coefficient -	Emissivity -	Inner diameter mm	Outer diameter mm
0.9	0.95	22	60

The properties of the pipe material used for the supply and return lines are listed in **Table 7**.

Table 7 Properties of pipe material

Inner diameter	Outer diameter	Density	Specific heat	Conductivity
mm	mm	kg/m³	J/kgK	W/Km
20	22	8600	382	300

Properties of the heat carrier

A chemical analysis of the heat carrier TyfocorLS® yielded a mass fraction, $x_{m0} = 0.579$, for the system with conventional selective absorbers and, $x_{m0} = 0.577$, for the system with thermochromic absorbers. The saturation temperature of the mixture is calculated based on the simplifying assumption of an ideal two-component mixture of water and propylene glycol using properties listed in Table 8. Within the temperature range considered here, the vapor pressure is sufficiently well described by a power function,

$$p_v = a\vartheta^b . \quad (96)$$

Preprints (www.preprints.org) | NOT PEER-REVIEWED | Posted: 30 December 2020 doi:10.20944/preprints202012.0750.v1

The coefficients listed in Table 8 are based on data from Steele, W. V. et al. [37] for propylene glycol , from D'Ans J., Lax E., Blachnik R. [38] for water and from the data sheet of TyfocorLS® [39].

Table 8 Properties of water and propylene glycol

	Molar mass	Coefficients for vapor pressure in Pa	
Component	kg/kmol	a	b
Water	18.02	$0.7517 \cdot 10^{-3}$	4.047
Propylene-glycol	76.1	$1.8745 \cdot 10^{-8}$	5.601
TyfocorLS	-	$0.7517 \cdot 10^{-3}$	4.225

The specific heat capacity, density and viscosity are approximated by functions based on D'Ans et al. [38] for water and the data sheet of TyfocorLS® [39]. The surface tension of TyfocorLS® is modelled based on experimental data presented by Chang, *et al.* [40] for a binary mixture of propylene glycol with a molar fraction x=0.85 of water.

$$\sigma = 0.0373 - 4.08 \cdot 10^{-5} \vartheta \quad \mathrm{N/m} \tag{97}$$

Preprints (www.preprints.org) | NOT PEER-REVIEWED | Posted: 30 December 2020 doi:10.20944/preprints202012.0750.v1

Appendix B

Table 9 Symbols and indices

Symbol	Unit		Symbol	Unit	
A	m²	Area	V	m³	Volume
a_1	W/Km²	Heat loss coefficient	$\dot{W}$	W	Work rate
a_2	W/K²m²	Heat loss coefficient	w	m/s	Velocity
c	J/kgK	Specific heat capacity	w_{gj}	m/s	Drift velocity
C	J/K	Heat capacity	x	m	Location of steam front
C_0	-	Distr. parameter	$\dot{x}$	m/s	Velocity of steam front
d	m	Diameter	x	-	Molar fraction
D	m	Outer diameter	x_m	-	Mass fraction
G	W/m²	Solar irradiation	**Greek symbols**		
h_C	m	Height difference	α	-	Steam power exponent
h	J/kg	Specific enthalpy	α	-	Absorption coefficient
h_v	J/kg	Spec. evap. enthalpy	α_c	W/Km²	Conv. heat transfer coeff.
j	m/s	Superficial velocity	α_r	W/Km²	Rad. heat transfer coeff.
K	-	Correction factor	β	1/K	Expansion coefficient
L	m	Char. length	β	-	Steam-filled fraction
l	m	Length	γ	-	View factor
m	kg	Mass	δ	-	Distribution parameter
$\dot{m}$	kg/s	Mass flow	ε	-	Emissivity
n	-	Number of nodes	η	-	Efficiency
n_C	-	Number of collectors	λ	W/Km	Heat conductivity
			ν	m²/s	Kinemat. viscosity
P_v	W	Steam power	ρ	Kg/m³	Density
p	Pa	Pressure	σ	Pa	Surface tension
$\dot{Q}$	W	Enthalpy change, gain	τ	s	Interval
R_D	-	Displacement ratio	φ	rad	Inclination angle
S	m²	Surface	**Dimensionless numbers**		
T	K, °C	Temperature	Nu	-	Nusselt number
U_L	W/Km²	Heat loss coefficient	Pr	-	Prandtl number
U_{gj}	m/s	Average drift velocity	Re	-	Reynolds number
u	J/kg	Specif. inner energy	Ra	-	Rayleigh number

Subscripts			
a	Ambient	i,k,q	Indices
C	Collector		
F	Field, array	S	Stagnation
G	Glycol	s	Saturation
g,l	Gas, liquid phase	t	Tube, pipe
H,b	Bottom header	v	Vapor
H,t	Top header	W	Water

Preprints (www.preprints.org) | NOT PEER-REVIEWED | Posted: 30 December 2020 doi:10.20944/preprints202012.0750.v1

i	Insulation	WG	Water-Glycol mixture
M	Meander	α	Inlet
m	Mean value	ω	Outlet

Constants

g	Acceleration of gravity	9.81	m/s^2
σ	Stefan-Boltzmann constant	$5.67037 \cdot 10^{-8}$	W/K^4m^2

References

1. Terschueren, K.-H. Solaranlagen zur Brauchwassererwärmung, Anlagenkomponenten, Installation, Inbetriebnahme, Betriebsverhalten, Teil 2. *IKZ-Haustechnik* **1996**, *Ausgabe 4*.
2. Eismann, R.; von Felten, P. *Stillstandsverhalten von Solaranlagen, Publikation 195200*; 195200; Bern, 1998.
3. Hausner, R.; Fink, C. Stagnation behaviour of solar thermal systems. In Proceedings of ISES Europe Solar Congress, Copenhagen.
4. Hausner, R.; Fink, C. *Stagnation behaviour of solar thermal systems - A Report of IEA SHC - Task 26 - Solar Combisystems*; 2002.
5. Lustig, K. Experimentelle Untersuchungen zum Stillstandsverhalten thermischer Solaranlagen. Dissertation, Univ. Karlsruhe, Karlsruhe, 2002.
6. Streicher, W. Minimising the risk of water hammer and other problems at the beginning of stagnation of solar thermal plants — a theoretical approach. *Solar Energy* **2001**, *69, Supplement 6*, 187-196.
7. Hausner, R.; Fink, C.; Wagner, W.; Riva, R.; Hillerns, F. *Entwicklung von thermischen Solarsystemen mit unproblematischem Stagnationsverhalten*; Wien, 2003.
8. Rommel, M.; Siems, T.; Schüle, K.; Mehnert, S.; Becker, R. Wieviel Dampf produziert ein Kollektor im Stillstandsfall? In Proceedings of 15. Symposium Thermische Solarenergie, Bad Staffelstein.
9. Rommel, M.; Siems, T.; Schüle, K.; Mehnert, S.; Thoma, C. *Schlussbericht zum Teilprojekt: Entwicklung von Techniken zur Beherrschung des Stillstandsbetriebes*; Fraunhofer Gesellschaft für solare Energiesysteme ISE: Freiburg, 2007.
10. Scheuren, J.; Kirchner, M.; Eisenmann, W. Reduction of Stagnation Load of Large-Scale Collector Arrays. In Proceedings of Proceedings of the EuroSun.
11. Scheuren, J. Untersuchungen zum Stagnationsverhalten solarthermischer Kollektorfelder. Universität Kassel, Fachbereich Maschinenbau: Kassel University Press, 2008.
12. Harrison, S.; Cruickshank, C.A. A review of strategies for the control of high temperature stagnation in solar collectors and systems. *Energy Procedia* **2012**, *30*, 793-804.
13. Frank, E.; Mauthner, F.; Fischer, S. *Overheating prevention and stagnation handling in solar process heat applications*; Technical Report A.1.2; 2015.
14. Eismann, R. Thermohydraulik von Solaranlagen. Dissertation, Eidgenössische Technische Hochschule ETH Zürich, Zürich, 2014.
15. Freixa, J.; Kim, T.-W.; Manera, A. Thermal-hydraulic analysis of an intermediate LOCA test at the ROSA facility including uncertainty evaluation. *Nuclear Engineering and Design* **2012**, *249*, 97-103, doi:https://doi.org/10.1016/j.nucengdes.2011.08.061.
16. U.S.NRC. *TRACE V5. 0 Theory Manual. Field Equations, Solution Methods, and Physical Models*; Division of Risk Assessment and Special Projects, Office of Nuclear Regulatory Research, US Nuclear Regulatory Commission: Washington, DC, 2007.
17. Eismann, R.; Föller, F.; Witzig, A. *Programm THD: Thermohydraulisches Dimensionierungsprogramm für Solaranlagen. Schlussbericht*; Bundesamt für Energie BFE: Bern, 2017.

Preprints (www.preprints.org) | NOT PEER-REVIEWED | Posted: 30 December 2020 doi:10.20944/preprints202012.0750.v1

18. Müller, S.; Reineke-Koch, R.; Giovannetti, F.; Hafner, B. Experimental Investigations on the Stagnation Behavior of Thermochromic Flat Plate Collectors. In Proceedings of EuroSun, Rapperswil, Switzerland.
19. CEN. EN-12975-2, Thermische Solaranlagen und ihre Bauteile – Kollektoren. In *Teil 2: Prüfverfahren*, DIN EN: 2006; Vol. 12975.
20. Eismann, R. Accurate analytical modeling of flat plate solar collectors: Extended correlation for convective heat loss across the air gap between absorber and cover plate. *Solar Energy* **2015**, *122*, 1214-1224, doi:https://doi.org/10.1016/j.solener.2015.10.037.
21. Armacell. HT/ArmaFlex - The flexible insulation for high temperature applications. Availabe online: https://local.armacell.com/fileadmin/cms/uk/products/en/HTArmaFlexRangeUKROI.pdf (accessed on Nov. 18).
22. Adelard, L.; Pignolet-Tardan, F.; Mara, T.; Lauret, P.; Garde, F.; Boyer, H. Sky temperature modelisation and applications in building simulation. *Renewable Energy* **1998**, *15*, 418-430, doi:10.1016/s0960-1481(98)00198-0.
23. Churchill, S.W. A comprehensive correlating equation for laminar, assisting, forced and free convection. *AIChE Journal* **1977**, *23*, 10-16, doi:10.1002/aic.690230103.
24. Churchill, S.W.; Chu, H.H. Correlating equations for laminar and turbulent free convection from a horizontal cylinder. *International journal of heat and mass transfer* **1975**, *18*, 1049-1053.
25. Gnielinski, V. Berechnung mittlerer Wärme- und Stoffübergangskoeffizienten an laminar und turbulent überströmten Einzelkörpern mit Hilfe einer einheitlichen Gleichung. *Forsch Ingenieurwes* **1975**, *41*, 145-153, doi:10.1007/BF02560793.
26. Tetsu, F.; Haruo, U. Laminar natural-convective heat transfer from the outer surface of a vertical cylinder. *International Journal of Heat and Mass Transfer* **1970**, *13*, 607-615, doi:http://dx.doi.org/10.1016/0017-9310(70)90155-9.
27. Raithby, G.D.; Hollands, K.G.T. A General Method of Obtaining Approximate Solutions to Laminar and Turbulent Free Convection Problems. *Advances in Heat Transfer* **1975**, *11*, 265-315, doi:10.1016/S0065-2717(08)70076-5.
28. Dropkin, D.; Somerscales, E. Heat transfer by natural convection in liquids confined by two parallel plates which are inclined at various angles with respect to the horizontal. **1965**.
29. Zuber, N.; Findlay, N.A. Average Volumetric Concentration in Two-Phase Systems. *Transactions of the ASME Ser. C, Journal of Heat Transfer* **1965**, *87*, 453-468.
30. Coddington, P.; Macian, R. A study of the performance of void fraction correlations used in the context of drift-flux two-phase flow models. *Nuclear Engineering and Design* **2002**, *215*, 199-216, doi:http://dx.doi.org/10.1016/S0029-5493(01)00503-9.
31. Choi, J.; Pereyra, E.; Sarica, C.; Park, C.; Kang, J. An Efficient Drift-Flux Closure Relationship to Estimate Liquid Holdups of Gas-Liquid Two-Phase Flow in Pipes. *Energies* **2012**, *5*, 5294-5306.
32. Kirkup, L.; Frenkel, R. An Introduction to Uncertainty in Measurement: Using the GUM (Guide to the Expression of Uncertainty in Measurement) Cambridge University Press. *Cambridge, UK* **2006**.
33. Kovacs, P. *A guide to the standard EN 12975*; SP – Technical Research Institute of Sweden: 28.05.2012, 2012.
34. Chexal, B.; Lellouche, G.; Horowitz, J.; Healzer, J. A void fraction correlation for generalized applications. *Progress in Nuclear Energy* **1992**, *27*, 255-295, doi:http://dx.doi.org/10.1016/0149-1970(92)90007-P.

Preprints (www.preprints.org) | NOT PEER-REVIEWED | Posted: 30 December 2020 doi:10.20944/preprints202012.0750.v1

35. Bhagwat, S.M.; Ghajar, A.J. A flow pattern independent drift flux model based void fraction correlation for a wide range of gas–liquid two phase flow. *International Journal of Multiphase Flow* **2014**, *59*, 186-205, doi:http://dx.doi.org/10.1016/j.ijmultiphaseflow.2013.11.001.
36. Eismann, R. Cost reduction of solar thermal plants by advanced thermalhydraulic design methods. In Proceedings of CISBAT 2019, Lausanne.
37. Steele, W.V.; Chirico, R.D.; Knipmeyer, S.E.; Nguyen, A. Measurements of Vapor Pressure, Heat Capacity, and Density along the Saturation Line for ε-Caprolactam, Pyrazine, 1,2-Propanediol, Triethylene Glycol, Phenyl Acetylene, and Diphenyl Acetylene. *Journal of Chemical & Engineering Data* **2002**, *47*, 689-699, doi:10.1021/je010085z.
38. D'Ans, J.; Lax, E.; Blachnik, R. *Taschenbuch für Chemiker und Physiker: Band 3: Elemente, anorganische Verbindungen und Materialien, Minerale: Bd. III*; Springer: Berlin, Heidelberg, 1998.
39. TYFOROP. Technical Information: TYFOCOR LS. Availabe online: https://www.tyfo.de/uploads/TI/Ti_TYFOCOR-LS_gb.pdf (accessed on
40. Chang, C.-W.; Hsiung, T.-L.; Lui, C.-P.; Tu, C.-H. Densities, surface tensions, and isobaric vapor–liquid equilibria for the mixtures of 2-propanol, water, and 1,2-propanediol. *Fluid Phase Equilibria* **2015**, *389*, 28-40, doi:https://doi.org/10.1016/j.fluid.2014.12.040.